

DISSERTATIONES PHYSICAE UNIVERSITATIS TARTUENSIS

80

NIINA VOROPAJEVA

Elementary excitations near the boundary
of a strongly correlated crystal



TARTU UNIVERSITY PRESS

The study was carried out at the Institute of Physics, University of Tartu.

The dissertation was admitted on September 9, 2011 in partial fulfillment of the requirements for the degree of Doctor of Philosophy in Physics, and allowed for defense by the Council of the Institute of Physics, University of Tartu.

Supervisors: Dr. Alexei Sherman, Institute of Physics, University of Tartu, Tartu, Estonia.

Opponents: Dr. Andrei Mikheenkov, Institute for High Pressure Physics, Russian Academy of Sciences, Troitsk, Russian Federation
Moscow Institute of Physics and Technology,
Dolgoprudny, Russian Federation

Dr. Mihhail Klopov
Institute of Physics, Technical University of Tallinn, Estonia

Defence: November 15, 2011, University of Tartu, Estonia.

This work has been supported by Graduate School on Functional Materials and Technologies (GSFMT), University of Tartu and Tallinn University of Technology,

EU Social Funds project 1.2.0401.09-0079



European Union
European Social Fund



Investing in your future

ISSN 1406–0647

ISBN 978–9949–19–856–6 (trükis)

ISBN 978–9949–19–857–3 (PDF)

Autoriõigus Niina Voropajeva, 2011

Tartu Ülikooli Kirjastus

www.tyk.ee

Tellimus nr 629

*to Niina Grigorjeva,
in memoriam*

Contents

List of publications	8
1 Introduction	10
2 Theoretical overview	13
2.1 The retarded Green's function	13
2.2 The Matsubara Green's function	14
2.3 The Hubbard model	16
2.4 The t - J model	17
3 The t-J model on a semi-infinite 2D lattice	20
3.1 From the Hubbard model to the t - J model	20
3.2 The spin-wave approximation	23
4 Magnetic excitations and correlations: a semi-infinite 2D/3D lattice	27
4.1 The Hamiltonian	27
4.2 The magnon Green's function and its equation of motion	28
4.3 The magnon Green's function $\hat{D}^{(0)}$	30
4.4 The magnon spectrum	33
4.5 Spin correlations	35
5 Hole excitations: a semi-infinite 2D lattice	40
5.1 The Dyson equation	40
5.2 The hole spectrum	46
Summary	53
Summary in Estonian	55
Acknowledgements	57
Appendix: The relation between the spin correlation and Green's function	58
References	60
Publications	65
Curriculum Vitae	113
Curriculum Vitae in Estonian	114

List of publications

The thesis is based on the following papers:

- I N. Voropajeva, A. Sherman, *Spin correlations near the surface of a three-dimensional Heisenberg antiferromagnet*, Phys. Lett. A **373**, 3473 (2009).
- II A. Sherman, N. Voropajeva, *Excitations near the boundary between a metal and a Mott insulator*, Int. J. Mod. Phys. B **24**, 979 (2010).
- III N. Voropajeva, A. Sherman, *Near-boundary and bulk regions of a semi-infinite two-dimensional Heisenberg antiferromagnet*, Mod. Phys. Lett. B **24**, 2327 (2010).
- IV A. Sherman, N. Voropajeva, *t-J model on a semi-infinite lattice*, J. Phys.: Condens. Matter **22**, 275603 (2010).

List of other publications:

- 1. N. Voropajeva, T. Örd, *Correlation in the velocity of a Brownian particle induced by frictional anisotropy and magnetic field*, Phys. Lett. A **372**, 2167 (2008).
- 2. A. Vargunin, T. Örd, R. Tammelo, N. Voropajeva, *On phase transition and the critical size in spatially restricted systems*, J. Phys.: Condens. Matter **20**, 362202 (2008).

Presentations at international conferences:

- 1. N. Voropajeva, A. Sherman, *Elementary excitations near the boundary of a strongly correlated crystal* (oral presentation), Workshop "Korrelationstage", Dresden, Germany, February 28 - March 4, 2011
- 2. N. Voropajeva, A. Sherman, *Near-boundary and bulk regions of semi-infinite two- and three-dimensional Heisenberg antiferromagnets* (poster presentation), The third Bilateral Estonian-German Workshop on Strong Nonlinear Vibronic and Electronic Interactions in Solids, Cottbus, Germany, June 13-15, 2011.
- 3. N. Voropajeva, A. Sherman, *Peculiarities of the hole spectral function near the boundary of a strongly correlated metal* (poster presentation), The third Bilateral Estonian-German Workshop on Strong Nonlinear Vibronic and Electronic Interactions in Solids, Cottbus, Germany, June 13-15, 2011.

Contributions to presentations at international conferences:

1. A. Sherman, N. Voropajeva, M. Schreiber, *Excitations near the boundary between a metal and a Mott insulator* (oral presentation), The second Bilateral Estonian-German Workshop on Strong Nonlinear Vibronic and Electronic Interactions in Solids, Cottbus, Germany, 21-23 May, 2009.

Author's contribution

The research of the author has given an essential contribution to all these publications. She participated in the development and verification of models and methods of their solution, in the analytical and numerical calculations and in the analysis of obtained results. The texts of the articles I and III were mainly written by the author; her contribution in writing the articles II and IV was also important

1 Introduction

There are strong reasons to believe that the near-boundary region of a solid has properties, which differ from properties of its bulk. If the boundary arose as a consequence of the cleavage of a solid parallel to an atomic layer, atoms may be shifted from their equilibrium positions, steps and other defects of crystal structure may appear. Even in the absence of such imperfections, the lack of neighbors on one side of the boundary leads to an increase of distances between atomic planes with the respective changes in matrix elements - the phenomenon called the relaxation in surface physics [1]. Moreover, in some cases boundary atoms are reconstructed in a structure with symmetry, which differs from the symmetry of the bulk. For the behavior of charge carriers broken atomic bonds, which exist on the boundary, are of primary importance. In the case of metals and narrow gap semiconductors these bonds lead to the appearance of the Shockley boundary states [2, 3]. Analogous states in transition metals and wide gap semiconductors are called Tamm boundary states [4, 5]. Boundary states can also be observed in ionic crystals [6, 7]. The electronic density in these boundary states is located in several near-boundary layers in contrast to the bulk states, in which the density is nonzero throughout the crystal. The boundary states resemble localized states, which appear near point defects in solids. These states are located in some region around the defect, where the magnitude of bulk states is suppressed [8–10]. This leads to the situation in which the defect neighborhood and the rest of the crystal constitute two systems with different dominant excitations. Thus, the crystal boundary behaves in some respects similar to the defect [1].

In recent years, an active interest has been taken in the electronic properties of heterostructures and surfaces of strongly correlated materials [11]. Looking for new effects and their possible applications a wide variety of systems has been investigated both experimentally and theoretically. In particular, it was established that the interface of Mott and band insulators can demonstrate metallic behavior [12–15]. Similar behavior is expected for the interface of two Mott insulators [16]. With lowering temperature, this two-dimensional metal becomes superconducting and the transition has some properties of the Berezinsky-Kosterlitz-Thouless transition [17, 18]. The conduction layer can be manipulated by gate voltages which thereby provide a way for carrier doping by electric field, in a disorder-free way, and is promising for new devices [19]. Notice also experiments with ultracold atoms where the coexistence of several phases with phase boundaries is often observed [20, 21].

Theoretical studies of charge excitations near the boundary of a crystal with strong electron correlations have been carried out mainly in the framework of the two- (2D) and three-dimensional (3D) Hubbard model. For this purpose different approximate methods have been used, including the slave boson method [22], the perturbation theory [23] and the dynamical mean-field theory [24–26]. In these works, the case of half-filling was considered, when

strong electron correlations cause the antiferromagnetic ordering of the crystal [27]. However, approximations used in the mentioned works did not take into account the ordering and the interaction of electrons with respective magnetic excitations. One of the results obtained in [22–26] for uniform model parameters is that on the surface layer the quasiparticle weight is smaller than the bulk value. The reason is a reduced surface coordination number which implies a lower kinetic energy and consequently effectively stronger correlation effects at the surface.

As mentioned above, crystals with strong electron correlations are magnetic materials, and their magnetic excitations are usually described in the framework of the quantum Heisenberg model [28]. For this model, the influence of boundaries on the spectrum and observables has been studied in one [29, 30] and two [31–33] dimensions. One of the results obtained in the 2D case with the use of Monte Carlo simulations [31], the spin-wave approximation [32] and the series expansion [33] is the increased absolute values of the nearest-neighbor spin correlations near the boundary of the antiferromagnet. With distance from the surface the correlations tend rapidly to their bulk value revealing some oscillations. The arising pattern of spin correlations was called the comb structure. It was argued that the increased surface correlations can be a manifestation of a short-range valence-bond-solid ordering in the Néel phase [32, 33].

The thesis is devoted to the investigation of the influence of a crystal boundary on elementary excitations in a strongly correlated crystal. It is well known that in such a crystal the interaction between spin excitations and charge carriers is of primary importance in determining their dispersion [28, 34]. To take proper account of this interaction the t - J model is applied for the description of these excitations. This is one of the most frequently used models for strongly correlated crystals, in particular, for cuprate perovskites. In the undoped case, the model reduces to the Heisenberg model, which is investigated at first. The cases of two and three dimensions were considered. It was shown that in the d -dimensional Heisenberg antiferromagnet the boundary leads to the appearance of two regions with drastically different spin excitations - a near-boundary region with $(d-1)$ -dimensional magnons and a bulk with d -dimensional standing spin waves. Spin correlations in the near-boundary region are increased in comparison with the bulk due to the decreased dimensionality of spin excitations in the former area. Thus, to a great extent the behavior of spin excitations near the crystal boundary resembles electrons near a point defect [8–10] - in both cases the perturbation divides the crystal into two regions with different excitations. Some of these excitations are localized in the perturbed region, while the other are the bulk excitations. Considering the case of small hole concentrations in the two-dimensional crystal it was shown that the near-boundary region is depleted of carriers. In the considered system, the carriers are spin polarons - holes surrounded by a cloud of magnons [28, 34]. The approach of the spin polaron to the boundary is accompanied with a deformation of the

magnon cloud, which is energetically unfavorable and leads to the depletion. No boundary states were found for holes - in the considered case of strong electron correlations the interaction with spin excitations has a larger impact on the carrier properties than dangling bonds on the boundary. Due to the broken translational symmetry in the direction perpendicular to the boundary the hole spectral function is characterized by components of the wave vector, which are parallel to the boundary, and by the distance of an atomic row from the boundary. The depletion of carriers in the near-boundary region means differences in the spectral functions belonging to various rows. As a consequence, the spectral function of the boundary row differs considerably from its bulk shape.

The structure of the thesis is the following. In Chapter 2 a theoretical overview of the retarded and Matsubara Green's functions as well as of two main models of strongly correlated systems, the Hubbard and the t - J models, is given. In Chapter 3 the t - J Hamiltonian on a semi-infinite two-dimensional lattice is derived from the Hubbard model in the limit of large Hubbard repulsions and small hole concentrations using the spin-wave approximation. In Chapter 4 the influence of the boundary on magnetic excitations and nearest-neighbor spin correlations of a semi-infinite two- and three-dimensional spin- $\frac{1}{2}$ Heisenberg antiferromagnet is investigated. Square and simple cubic lattices are considered with the boundary oriented perpendicular to one of the crystal axes. The spin-wave approximation is applied for zero temperature. In Chapter 5 the influence of the boundary on charge carriers in a semi-infinite two-dimensional t - J model is studied. For this purpose, the hole spectral function is calculated using the spin-wave and non-crossing approximations for the case of small hole concentrations and zero temperatures.

2 Theoretical overview

2.1 The retarded Green's function

Let us introduce two arbitrary operators $A(t)$ and $B(t')$ in the Heisenberg representation:

$$A(t) = e^{iHt} A e^{-iHt}, \quad B(t') = e^{iHt'} B e^{-iHt'},$$

where H is the Hamiltonian of a system.

Lets us define a double-time retarded Green's function as follows [35]:

$$G(t, t') = \langle\langle A(t)|B(t') \rangle\rangle_t = -i\theta(t - t') \langle[A(t), B(t')]_\eta\rangle, \quad (2.1)$$

where $[A(t), B(t')]_\eta = A(t)B(t') - \eta B(t')A(t)$. Usually $\eta = 1$ is chosen if operators satisfy the Boson commutation relations, and $\eta = -1$ is taken if operators satisfy the Fermion commutation relations. In Eq. (2.1), averaging is performed over the Gibbs canonical ensemble: $\langle\dots\rangle = Z^{-1}\text{Sp}(e^{-H\beta}\dots)$, $Z = \text{Sp}(e^{-H\beta})$ is the partition function, β is the inverse value of the temperature in energy units, and $\theta(t)$ is the Heaviside function.

If the Hamiltonian does not depend on time, the retarded Green's function depends only on the time difference, $G(t, t') = G(t - t')$. This property can be verified using trace invariance with respect to cyclic permutation of multipliers. Therefore, it is convenient to take one of the temporal arguments equaling to zero: $G(t) \equiv G(t, 0)$.

To obtain the equation of motion describing evolution of Green's function let us differentiate it with respect to the time t

$$i \frac{dG(t)}{dt} = \frac{d\theta(t)}{dt} \langle[A(t), B]_\eta\rangle + \theta(t) \left\langle \left[\frac{dA(t)}{dt}, B \right] \right\rangle.$$

Taking into account that $\frac{d\theta(t)}{dt} = \delta(t)$, the known property of Dirac's delta function, $\delta(t - t_0)f(t) = \delta(t - t_0)f(t_0)$ and the equation of motion for an operator in the Heisenberg representation,

$$i \frac{dA(t)}{dt} = [A(t), H],$$

one arrives at the equation of motion for Green's function

$$i \frac{dG(t)}{dt} = \delta(t) \langle[A, B]_\eta\rangle + \langle\langle[A, H]|B\rangle\rangle. \quad (2.2)$$

The Fourier transform of Green's function is defined as follows:

$$G(\omega) = \int_{-\infty}^{\infty} dt e^{i\omega t} G(t). \quad (2.3)$$

The retarded Green's function is an analytical function in the upper half-plane and has its poles, cuts, and branch points in the lower half-plane and on the real axis. The real and imaginary parts of the energies of the poles define energies and dampings of quasiparticles (elementary excitations), respectively.

2.2 The Matsubara Green's function

Let us introduce two arbitrary operators $A(\tau)$ and $B(\tau')$,

$$A(\tau) = e^{\tau H} A e^{-\tau H}, \quad B(\tau') = e^{\tau' H} B e^{-\tau' H}.$$

The Matsubara Green's function at non-zero temperatures is defined as follows [36, 37]:

$$G(\tau, \tau') = -\langle \mathcal{T} A(\tau) B(\tau') \rangle, \quad (2.4)$$

where \mathcal{T} is the time-ordering operator that arranges other operators from right to left in ascending order of times. In the case of Fermi operators their permutation caused by the time ordering leads to the change of sign in the expression.

As follows from the definition (2.4), Matsubara Green's functions depends only on the time difference $\bar{\tau} = \tau - \tau'$ and satisfy the condition $G(\bar{\tau} < 0) = \mp G(\bar{\tau} + \beta)$, where the upper and lower signs corresponds to Fermi and Bose operators, respectively. Therefore, it is convenient to take one of temporal arguments equaling to zero: $G(\tau) \equiv G(\tau, 0)$, where $\tau \in [0, \beta]$.

If the particles in a system are not free it is convenient to use the interaction representation of the quantum field theory [38]. If we separate the Hamiltonian into two parts,

$$H = H_0 + H_{int},$$

where H_0 is an exactly solvable unperturbed part, while H_{int} is a perturbation, then we can introduce an arbitrary operator $\tilde{A}(\tau)$ in the interaction representation,

$$\tilde{A}(\tau) = e^{\tau H_0} A e^{-\tau H_0}.$$

Also for this purpose we introduce the matrix $\mathcal{G}(\tau)$ ($0 < \tau < \beta$), the analogue

of the S -matrix of the field theory, which is defined as

$$\mathcal{G}(\tau) = \mathcal{T} \exp \left\{ - \int_0^\beta \tilde{H}_{int}(\tau') d\tau' \right\}, \quad \tilde{H}_{int}(\tau) = e^{\tau H_0} H_{int} e^{-\tau H_0}. \quad (2.5)$$

The expression for Green's function in the interaction representation may be written via the \mathcal{G} matrix (2.5) as

$$G(\tau) = - \frac{\langle \mathcal{T}(\tilde{A}(\tau) B \mathcal{G}(\beta)) \rangle_0}{\langle \mathcal{G}(\beta) \rangle_0}, \quad (2.6)$$

where the subscript "0" near the angular brackets denotes that the averaging is determined by the non-interacting Hamiltonian H_0 .

If the interactions between particles are weak, the expression for the Matsubara Green's function (2.6) in the interaction representation enables us to write the perturbation theory series in powers of interaction Hamiltonian \tilde{H}_{int} .

The interaction Hamiltonian appears in the Green's function only via the \mathcal{G} matrix (2.5). Expanding the exponent in the right-hand side of Eq. (2.5) in powers of $\tilde{H}_{int}(\tau)$, we get

$$\mathcal{G} = \sum_{n=0}^{\infty} \frac{(-1)^n}{n!} \int_0^\beta \dots \int_0^\beta d\tau_1 \dots d\tau_n \mathcal{T}(\tilde{H}_{int}(\tau_1) \dots \tilde{H}_{int}(\tau_n)). \quad (2.7)$$

Substituting this expansion in the numerator of Green's function (2.6), we get the perturbation theory series

$$G(\tau) = - \frac{1}{\langle \mathcal{G}(\beta) \rangle_0} \sum_{n=0}^{\infty} \frac{(-1)^n}{n!} \int_0^\beta \dots \int_0^\beta d\tau_1 \dots d\tau_n \langle \mathcal{T} \tilde{A}(\tau) B \tilde{H}_{int}(\tau_1) \dots \tilde{H}_{int}(\tau_n) \rangle_0.$$

After applying Wick's theorem [39], the Matsubara Green's function can be reduced to the evaluation of all connected diagrams

$$G(\tau) = - \sum_{n=0}^{\infty} \frac{(-1)^n}{n!} \int_0^\beta \dots \int_0^\beta d\tau_1 \dots d\tau_n \langle \mathcal{T} \tilde{A}(\tau) B \tilde{H}_{int}(\tau_1) \dots \tilde{H}_{int}(\tau_n) \rangle_{0,c}, \quad (2.8)$$

where the subscript "c" points to this limitation. Each diagram is evaluated as a function of τ , and then one takes the Fourier transform

$$G(n) \equiv G(i\omega_n) = \int_0^\beta d\tau G(\tau) e^{i\omega_n \tau}, \quad \omega_n = \begin{cases} (2n+1)\pi T & \text{for fermions,} \\ 2n\pi T & \text{for bosons,} \end{cases} \quad (2.9)$$

where n is an integer and the shorthand symbol for the Matsubara frequency ω_n . The terms in series yield self-energy diagrams, which may be collected into the Dyson equation (the self-energy equation)

$$G(n) = G^{(0)}(n) - G^{(0)}(n)\Sigma(n)G(n), \quad (2.10)$$

where $G^{(0)}(n)$ is the zeroth-order (non-interacting) Green's function and the function $\Sigma(n)$ is called the self-energy.

In order to transform the Dyson equation to real frequencies one needs to perform the analytic continuation

$$i\omega_n \rightarrow \omega + i\eta, \quad \eta \rightarrow +0.$$

This procedure gives the Dyson equation for Green's functions of section 2.1,

$$G(\omega) = G^{(0)}(\omega) + G^{(0)}(\omega)\Sigma(\omega)G(\omega). \quad (2.11)$$

2.3 The Hubbard model

Initially the Hubbard model [40] was introduced to describe magnetism in $3d$ transition metals and their compounds in an effort to overcome the contradictions between the itinerant (band) nature of d electrons and the presence of localized magnetic moments in such systems. Actually, as was shown by Hubbard [41], the applicability range of the model proved to be much broader: the model made it possible to describe the metal-insulator transitions initiated by changes in the Hamiltonian parameters. The success of the Hubbard model is due to its simplicity, and at the same time, to its rich content. The Hubbard model is able to describe a number of such nontrivial phenomena as ferromagnetism and antiferromagnetism, superconductivity, and Luttinger quantum liquid. The model Hamiltonian reads

$$H = t \sum_{ij\sigma} a_{i\sigma}^\dagger a_{j\sigma} + U \sum_i n_{i\uparrow} n_{i\downarrow}. \quad (2.12)$$

It contains a kinetic term describing the electron motion from site to site and the energy of repulsion at a single site. Here $a_{i\sigma}$ ($a_{j\sigma}^\dagger$) is the Fermi annihilation (creation) operator for an electron at site i with spin σ , $n_{i\sigma} = a_{i\sigma}^\dagger a_{i\sigma}$ is the number of electrons at a site i with the given spin σ , t is the hopping constant of an electron from one site to an adjacent site in the lattice, and U is the Coulomb repulsion between two electrons at the same site.

For sufficiently large $U \geq U_c \sim W$ the ground state of the system is an insulator state, while for $U < U_c$ it is a metallic state. Here W is the bandwidth of noninteracting electrons. The reason is that for large U the appearance of two electrons at the same site is energetically unfavorable and the initial band splits into two Hubbard sub-bands with a gap at the initial band center. Thus,

when the band is half-filled, the Fermi level is in the gap, and the ground state is an insulator state. The electrons become localized at the lattice sites and behave like localized magnetic moments with spin $S = 1/2$. An indirect exchange interaction arises between such electrons, so that the system in the insulator state is an antiferromagnet.

Of course, at deviations from the half-filled state of the band the system acquires finite conductivity, but clearly, there exists a strong interaction between the charge carrier and the magnetic order, which may initiate deviations from the Fermi-liquid behavior of the electron system. All these effects – the metal-insulator phase transition, the emergence of localized magnetic moments, and the deviations from the Fermi-liquid behavior – are manifestations of strong correlations existing in the system, i.e. the tendency of electrons to avoid each other.

2.4 The t - J model

This model was derived from the Hubbard model (2.12) in the limit of strong electron correlations, $W/U \ll 1$, and developed to describe electron motion in an antiferromagnetic matrix. It has gained popularity after P. Anderson [42] suggested that the electron properties of high- T_c superconductors of the metal-oxide group are described by the t - J Hamiltonian. To derive the t - J Hamiltonian one has to apply a canonical transformation which excludes the local two-electron states. Then after the use of the second-order perturbation theory in W/U , where the Coulomb term is taken as the zeroth-order Hamiltonian and the kinetic term is considered as a perturbation, one obtains the t - J Hamiltonian [43, 44] (see also the next chapter):

$$H = t \sum_{i \neq j, \sigma} (1 - n_{i, -\sigma}) a_{i\sigma}^\dagger a_{j\sigma} (1 - n_{j, -\sigma}) + \frac{J}{2} \sum_{i \neq j} \left(\mathbf{S}_i \mathbf{S}_j - \frac{1}{4} n_i n_j \right). \quad (2.13)$$

Here $n_i = \sum_{\sigma} n_{i\sigma}$ is the number of electrons at a site i , $J = 4t^2/U$ is the kinetic exchange (antiferromagnetic coupling) constant, and \mathbf{S}_i is the spin- $\frac{1}{2}$ operator at a site i . The factors $1 - n_{i, -\sigma}$ in Eq. (2.13) prevent double occupancy of the site i . Thus, the t - J model describes the motion of electrons from one unoccupied site to another.

In the case of half-filling, when the number of particles is equal to unity at each site,

$$n_{i\uparrow} + n_{i\downarrow} = 1,$$

the t - J model reduces to *the Heisenberg model*

$$H = J \sum_{ij} \left(\mathbf{S}_i \mathbf{S}_j - \frac{1}{4} n_i n_j \right). \quad (2.14)$$

Near half-filling in the spin-wave approximation the Hamiltonian of the t - J model on an infinite 2D lattice in momentum space reads [45]

$$\begin{aligned}
H &= \frac{Jz}{2} \sum_{\mathbf{k}} \left[2b_{\mathbf{k}}^{\dagger} b_{\mathbf{k}} + \gamma_{\mathbf{k}} \left(b_{\mathbf{k}} b_{-\mathbf{k}} + b_{-\mathbf{k}}^{\dagger} b_{\mathbf{k}}^{\dagger} \right) \right] \\
&+ \frac{tz}{\sqrt{N}} \sum_{\mathbf{k}\mathbf{q}} h_{\mathbf{k}}^{\dagger} h_{\mathbf{k}-\mathbf{q}} \left(\gamma_{\mathbf{k}} b_{-\mathbf{q}}^{\dagger} + \gamma_{\mathbf{k}-\mathbf{q}} b_{\mathbf{q}} \right). \tag{2.15}
\end{aligned}$$

Here $b_{\mathbf{k}}$ is the spin-wave operator, $h_{\mathbf{k}}$ is the hole annihilation operator, z is the number of the nearest neighbors (the coordination number), $\gamma_{\mathbf{k}} = z^{-1} \sum_{\mathbf{r}} e^{i\mathbf{k}\mathbf{r}}$, and \mathbf{r} is a nearest-neighbor vector. After applying the canonical (Bogoliubov) transformation

$$b_{\mathbf{k}} = u_{\mathbf{k}} \beta_{\mathbf{k}} + v_{\mathbf{k}} \beta_{-\mathbf{k}}^{\dagger} \tag{2.16}$$

to the new Bose operators $\beta_{\mathbf{k}}$, we arrive at the expression for the effective Hamiltonian

$$H = \sum_{\mathbf{k}} \omega_{\mathbf{k}} \left(\beta_{\mathbf{k}}^{\dagger} \beta_{\mathbf{k}} + \frac{1}{2} \right) + \frac{1}{\sqrt{N}} \sum_{\mathbf{k}\mathbf{q}} \left[\mathcal{M}_{\mathbf{q}}(\mathbf{k}) h_{\mathbf{k}}^{\dagger} h_{\mathbf{k}-\mathbf{q}} \beta_{\mathbf{q}} + \text{c.c.} \right]. \tag{2.17}$$

Here

$$\mathcal{M}_{\mathbf{q}}(\mathbf{k}) = zt(u_{\mathbf{q}} \gamma_{\mathbf{k}-\mathbf{q}} + v_{\mathbf{q}} \gamma_{\mathbf{k}}) \tag{2.18}$$

is the hole-spin-wave interaction amplitude, and

$$\begin{aligned}
u_{\mathbf{k}} &= \frac{1}{2} \left(\sqrt[4]{\frac{1-\gamma_{\mathbf{k}}}{1+\gamma_{\mathbf{k}}}} + \sqrt[4]{\frac{1+\gamma_{\mathbf{k}}}{1-\gamma_{\mathbf{k}}}} \right), & v_{\mathbf{k}} &= \frac{1}{2} \left(\sqrt[4]{\frac{1-\gamma_{\mathbf{k}}}{1+\gamma_{\mathbf{k}}}} - \sqrt[4]{\frac{1+\gamma_{\mathbf{k}}}{1-\gamma_{\mathbf{k}}}} \right), \\
\omega_{\mathbf{k}} &= Jz \sqrt{1-\gamma_{\mathbf{k}}^2}.
\end{aligned}$$

We see that near half-filling the Hamiltonian of the t - J model reduces to the spin-wave Hamiltonian of an antiferromagnet interacting with holes. This closely resembles the phonon polaron problem in a deformable lattice [46] – the spin waves play the role of the phonons. However, between the two problems there is an important distinction: Hamiltonian (2.17) has no bare term, $H_0 = \sum_{\mathbf{k}} \varepsilon_{\mathbf{k}} h_{\mathbf{k}}^{\dagger} h_{\mathbf{k}}$, for holes. The hole kinetic energy of the t - J model transforms into a term describing hole-magnon coupling. Since the interaction amplitude $\mathcal{M}_{\mathbf{q}}(\mathbf{k})$ is proportional to $t \gg J$, we are dealing with strong coupling.

The hole-magnon interaction leads to the dressing of holes with magnons. The combined quasiparticle is called the magnetic or spin polaron. Its dispersion is determined by the self-energy. Note that the interaction amplitude $\mathcal{M}_{\mathbf{q}}(\mathbf{k})$ vanishes at $\mathbf{q} = 0$ and $\mathbf{q} = (\pi, \pi)$; however, it becomes large at inter-

mediate values of the momentum transfer \mathbf{q} . This implies that the interaction between a hole and short-wavelength spin-waves plays an important role in the spin polaron problem. This means that the spin polaron is well localized in space.

Using the self-consistent Born approximation in the diagram technique one obtains the following self-energy equation for the case of one hole:

$$G(\mathbf{k}, \omega) = \frac{1}{\omega - \Sigma(\mathbf{k}, \omega) + i0} \quad (2.19)$$

with the self-energy

$$\Sigma(\mathbf{k}, \omega) = \frac{1}{N} \sum_{\mathbf{q}} \mathcal{M}_{\mathbf{q}}^2(\mathbf{k}) G(\mathbf{k} - \mathbf{q}, \omega - \omega_{\mathbf{q}}). \quad (2.20)$$

In this case, the spectral function consists of a narrow quasiparticle peak, which is well separated from a broad continuum. In the hole picture, the continuum is located on the high-energy side of the quasiparticle peak. The bandwidth of the quasiparticle states is of the order of J , and their contribution to the total intensity is in the region of J/t . The energy range occupied by the continuum is close to zt . States, which constitute the continuum, correspond to different excited states of the spin polaron, in particular, to the so called string states. The band of the quasiparticle states has minima at the wave vectors $(\pm\pi/2, \pm\pi/2)$, where the lattice spacing is set as a unit of length. Maxima of the band are located at $(0, 0)$ and (π, π) . In comparison with the dispersion along the line $(0, 0) - (\pi, \pi)$ the variation of the band energy along the boundaries of the magnetic Brillouin zone $(0, \pm\pi) - (\pm\pi, 0)$ is small.

3 The t - J model on a semi-infinite 2D lattice

3.1 From the Hubbard model to the t - J model

In this subsection the transformation of the Hubbard Hamiltonian to the t - J Hamiltonian is carried out for the case of a semi-infinite 2D square lattice. The case of small hole concentrations and strong correlations ($U \gg |t|$) is considered. A semi-infinite antiferromagnet is chosen to be located in the half-space $l_x \geq 0$ (a boundary is located along the Y crystallographic axis). We limit ourselves to the case of an idealized boundary: the variation of lattice spacing and model parameters near the boundary is neglected. The Hamiltonian reads

$$\begin{aligned}
 H_H = & t \sum_{l_y \sigma} \sum_{\delta, l_x \geq 0} a_{l_y + \delta, l_x \sigma}^\dagger a_{l_y l_x \sigma} + t \sum_{l_y \sigma} \sum_{l_x \geq 0} \left(a_{l_y, l_x + 1, \sigma}^\dagger a_{l_y l_x \sigma} + a_{l_y l_x \sigma}^\dagger a_{l_y, l_x + 1, \sigma} \right) \\
 & + U \sum_{l_y, l_x \geq 0} n_{l_y l_x, +1} n_{l_y l_x, -1} - \mu \sum_{l_y \sigma} \sum_{l_x \geq 0} n_{l_y l_x \sigma},
 \end{aligned} \tag{3.1}$$

where l_y and l_x are the vector components labeling sites of the crystal, $\delta = \pm 1$ (the lattice spacing is set as the unit of length), $\sigma = \pm 1$ is the spin projection, and μ is the chemical potential of electrons. Only the hopping between nearest-neighbor sites t is taken into account in Hamiltonian (3.1).

It is convenient to switch to the Hubbard operators [47, 48]

$$X_{\mathbf{M}}^{ij} = |\mathbf{M}i\rangle\langle\mathbf{M}j|, \quad \mathbf{M} = (l_x, l_y). \tag{3.2}$$

Here $|\mathbf{M}i\rangle$ denotes four possible site states - the unoccupied state ($i = 0$), the two singly occupied states ($i = \sigma$), and the doubly occupied state ($i = 2$). The Hubbard operator $X_{\mathbf{M}}^{ij}$ is a transition operator with the initial state $|\mathbf{M}j\rangle$ and the final state $|\mathbf{M}i\rangle$. The algebra of Hubbard operators is given by the following rules:

1. the multiplication rule

$$X_{\mathbf{M}}^{p_1 q_1} \cdot X_{\mathbf{M}}^{p_2 q_2} = |\mathbf{M}p_1\rangle\langle\mathbf{M}q_1| |\mathbf{M}p_2\rangle\langle\mathbf{M}q_2| = \delta_{q_1 p_2} X_{\mathbf{M}}^{p_1 q_2},$$

2. the commutation rule

$$\left[X_{\mathbf{M}_1}^{p_1 q_1}, X_{\mathbf{M}_2}^{p_2 q_2} \right]_{\pm} = \delta_{\mathbf{M}_1 \mathbf{M}_2} \left(\delta_{q_1 p_2} X_{\mathbf{M}_1}^{p_1 q_2} \pm \delta_{p_1 q_2} X_{\mathbf{M}_1}^{p_2 q_1} \right),$$

where $\left[X_{\mathbf{M}_1}^{p_1 q_1}, X_{\mathbf{M}_2}^{p_2 q_2} \right]_{\pm}$ denotes the anticommutator when both operators are of fermion type ($X_{\mathbf{M}}^{0\sigma}, X_{\mathbf{M}}^{\sigma 2}$ and their conjugates) and the commutator in other cases,

3. the sum rule (the completeness condition)

$$\sum_p X_M^{pp} = \sum_p |\mathbf{M}p\rangle\langle\mathbf{M}p| = 1.$$

All these rules are consequences of the definition of the Hubbard operators (3.2) and the condition that $\{|\mathbf{M}p\rangle\}$ is a complete set of orthogonal and normalized vectors.

The electron creation operator $a_{l_y l_x \sigma}^\dagger$, the electron annihilation operator $a_{l_y l_x \sigma}$, and the number operator $n_{l_y l_x \sigma}$ are connected with the Hubbard operators by the relations,

$$\begin{aligned} a_{l_y l_x \sigma} &= X_{l_y l_x}^{0\sigma} + \sigma X_{l_y l_x}^{-\sigma,2}, & a_{l_y l_x \sigma}^\dagger &= X_{l_y l_x}^{\sigma 0} + \sigma X_{l_y l_x}^{2,-\sigma}, \\ n_{l_y l_x \sigma} &= X_{l_y l_x}^{\sigma\sigma} + X_{l_y l_x}^{22}. \end{aligned} \quad (3.3)$$

Taking into account Eq. (3.3), the multiplication rule, the sum rule of the Hubbard operators and dropping a constant term, we get for the Hamiltonian

$$\begin{aligned} H_H &= H_0 + H_1 + H_2, \\ H_0 &= U \sum_{l_y, l_x \geq 0} X_{l_y l_x}^{22} - \mu \sum_{l_y, l_x \geq 0} \left(X_{l_y l_x}^{22} - X_{l_y l_x}^{00} \right), \\ H_1 &= t \sum_{l_y \sigma} \sum_{l_x \geq 0} \left(X_{l_y + \delta, l_x}^{\sigma 0} X_{l_y l_x}^{0\sigma} + X_{l_y + \delta, l_x}^{2,-\sigma} X_{l_y l_x}^{-\sigma,2} \right) \\ &\quad + t \sum_{l_y \sigma} \sum_{l_x \geq 0} \left(X_{l_y, l_x + 1}^{\sigma 0} X_{l_y l_x}^{0\sigma} + X_{l_y, l_x + 1}^{2,-\sigma} X_{l_y l_x}^{-\sigma,2} \right. \\ &\quad \left. + X_{l_y l_x}^{\sigma 0} X_{l_y, l_x + 1}^{0\sigma} + X_{l_y l_x}^{2,-\sigma} X_{l_y, l_x + 1}^{-\sigma,2} \right), \\ H_2 &= t \sum_{l_y \sigma} \sum_{l_x \geq 0} \sigma \left(X_{l_y + \delta, l_x}^{\sigma 0} X_{l_y l_x}^{-\sigma,2} + X_{l_y + \delta, l_x}^{2,-\sigma} X_{l_y l_x}^{0\sigma} \right) \\ &\quad + t \sum_{l_y \sigma} \sum_{l_x \geq 0} \sigma \left(X_{l_y, l_x + 1}^{\sigma 0} X_{l_y l_x}^{-\sigma,2} + X_{l_y, l_x + 1}^{2,-\sigma} X_{l_y l_x}^{0\sigma} \right. \\ &\quad \left. + X_{l_y l_x}^{\sigma 0} X_{l_y, l_x + 1}^{-\sigma,2} + X_{l_y l_x}^{2,-\sigma} X_{l_y, l_x + 1}^{0\sigma} \right). \end{aligned} \quad (3.4)$$

By analogy with an unbounded crystal [43, 49], in the case of strong electron correlations, $U \gg |t|$, and an electron filling less than half-filling, Hamiltonian (3.4) can be reduced to the Hamiltonian of the t - J model using a unitary transformation and a perturbation theory in powers of the small parameter t/U ,

$$\begin{aligned} H_{tJ} &= e^S H e^{-S} \approx H_0 + H_1 + H_2 + [S, H_0] + [S, H_1] + [S, H_2] \\ &\quad + \frac{1}{2} [S, [S, H_0]] + \dots \end{aligned} \quad (3.5)$$

In Eq. (3.5), H_0 is the zero-order term, while other terms in the right-hand side are of the first and second order in the parameter t/U . This unitary transformation has to remove terms of the first order in t which change the occupation of the Hubbard subbands. Terms of this type are collected in the part H_2 in Eq. (3.4). The operator S is looked for in the form

$$\begin{aligned}
S &= \xi \sum_{l_y \sigma} \sum_{l_x \geq 0} \sigma \left(X_{l_y+\delta, l_x}^{\sigma 0} X_{l_y l_x}^{-\sigma, 2} - X_{l_y+\delta, l_x}^{2, -\sigma} X_{l_y l_x}^{0\sigma} \right) \\
&+ \xi \sum_{l_y \sigma} \sum_{l_x \geq 0} \sigma \left(X_{l_y, l_x+1}^{\sigma 0} X_{l_y l_x}^{-\sigma, 2} - X_{l_y, l_x+1}^{2, -\sigma} X_{l_y l_x}^{0\sigma} \right) \\
&+ X_{l_y l_x}^{\sigma 0} X_{l_y, l_x+1}^{-\sigma, 2} - X_{l_y l_x}^{2, -\sigma} X_{l_y, l_x+1}^{0\sigma},
\end{aligned} \tag{3.6}$$

where the parameter ξ is determined from the condition

$$H_2 + [S, H_0] = 0, \tag{3.7}$$

which eliminates the mentioned terms from the transformed Hamiltonian (3.5). Substituting H_0 , H_2 (3.5), and S (3.6) into condition (3.7) and using the commutation rule of the Hubbard operators, we obtain that

$$[S, H_0] = \frac{\xi U}{t} H_2, \quad \xi = -\frac{t}{U}.$$

In the case of strong electron correlations, $U \gg |t|$, it is sufficient to leave terms up to the second order in t in the transformed Hamiltonian (3.5). If in addition we take into account condition (3.7) then the expression for Hamiltonian (3.5) is reduced to

$$H_{tJ} = H_0 + H_1 + [S, H_1] + \frac{1}{2}[S, H_2]. \tag{3.8}$$

In the case of an electron filling less than half-filling we retain terms of the Hamiltonian, which describe only processes in the lower Hubbard subband and we neglect terms containing the Hubbard operators $X^{2, -\sigma}, X^{-\sigma, 2}, X^{22}, X^{02}, X^{20}$. Since each term of the commutator $[S, H_1]$ contains such Hubbard operators, the commutator does not contribute to the Hamiltonian. After some mathematical manipulations, the Hamiltonian is reduced to

$$\begin{aligned}
H_{tJ} &= t \sum_{l_y \sigma} \sum_{l_x \geq 0} X_{l_y+\delta, l_x}^{\sigma 0} X_{l_y l_x}^{0\sigma} + t \sum_{l_y \sigma} \sum_{l_x \geq 0} \left(X_{l_y, l_x+1}^{\sigma 0} X_{l_y l_x}^{0\sigma} + X_{l_y, l_x+1}^{\sigma 0} X_{l_y l_x}^{0\sigma} \right) \\
&- \frac{2t^2}{U} \sum_{l_y, l_x \geq 0} \sum_{\sigma \sigma'} \sigma \sigma' \left(X_{l_y+1, l_x}^{\sigma \sigma'} X_{l_y l_x}^{-\sigma, -\sigma'} + X_{l_y, l_x+1}^{\sigma \sigma'} X_{l_y l_x}^{-\sigma, -\sigma'} \right) \\
&+ \mu \sum_{l_y, l_x \geq 0} X_{l_y l_x}^{00}.
\end{aligned} \tag{3.9}$$

Here we neglected three-site terms which describe an assistant hole hopping, as it is frequently done in the consideration of the t - J model. The third sum in the right-hand side of Eq. (3.9) can be rewritten in terms of the spin- $\frac{1}{2}$ operators $S_{\mathbf{M}}^{\pm}$, $S_{\mathbf{M}}^z$ and electron number operators if we use the relations

$$\begin{aligned} S_{l_y l_x}^+ &= X_{l_y l_x}^{1,-1}, & S_{l_y l_x}^- &= X_{l_y l_x}^{-1,1}, \\ S_{l_y l_x}^z &= \frac{1}{2} \left(X_{l_y l_x}^{11} - X_{l_y l_x}^{-1,-1} \right), & n_{l_y l_x} &= n_{l_y l_x \uparrow} + n_{l_y l_x \downarrow}. \end{aligned} \quad (3.10)$$

In these notations Hamiltonian (3.9) reads

$$\begin{aligned} H_{tJ} &= t \sum_{l_y \sigma} \sum_{\delta, l_x \geq 0} X_{l_y + \delta, l_x}^{\sigma 0} X_{l_y l_x}^{0 \sigma} + t \sum_{l_y \sigma} \sum_{l_x \geq 0} \left(X_{l_y, l_x + 1}^{\sigma 0} X_{l_y l_x}^{0 \sigma} + X_{l_y, l_x + 1}^{\sigma 0} X_{l_y l_x}^{0 \sigma} \right) \\ &+ J \sum_{l_y \sigma} \sum_{l_x \geq 0} \left(\mathbf{S}_{l_y + 1, l_x} \mathbf{S}_{l_y l_x} + \mathbf{S}_{l_y l_x + 1} \mathbf{S}_{l_y l_x} \right) \\ &- \frac{J}{4} \sum_{l_y \sigma} \sum_{l_x \geq 0} \left(n_{l_y + 1, l_x} n_{l_y l_x} + n_{l_y, l_x + 1} n_{l_y l_x} \right) + \mu \sum_{l_y, l_x \geq 0} X_{l_y l_x}^{00}. \end{aligned} \quad (3.11)$$

3.2 The spin-wave approximation

Further simplifications of the model Hamiltonian are connected with the existence of the long-range antiferromagnetic ordering in the crystal in the case of zero temperature and low doping. The long-range antiferromagnetic ordering allows us to use the spin-wave approximation which in applications to the t - J model was shown to give results in good agreement with exact diagonalization in the unbounded crystal [45, 50]. The spin-wave approximation is introduced using the following Holstein-Primakoff transformation [51]:

$$\begin{aligned} S_{l_y l_x}^+ &= P_{l_y l_x}^+ \varphi_{l_y l_x} b_{l_y l_x} + P_{l_y l_x}^- b_{l_y l_x}^\dagger \varphi_{l_y l_x}, \\ S_{l_y l_x}^- &= P_{l_y l_x}^- \varphi_{l_y l_x} b_{l_y l_x} + P_{l_y l_x}^+ b_{l_y l_x}^\dagger \varphi_{l_y l_x}, \\ S_{l_y l_x}^z &= e^{i\pi(l_y + l_x)} \left(\frac{1}{2} - b_{l_y l_x}^\dagger b_{l_y l_x} \right). \end{aligned} \quad (3.12)$$

Here the spin-wave operators $b_{l_y l_x}^\dagger, b_{l_y l_x}$ satisfy the Boson commutation relations and

$$P_{l_y l_x}^\pm = \frac{1}{2} \left[1 \pm e^{i\pi(l_x + l_y)} \right], \quad \varphi_{l_y l_x} = \sqrt{1 - b_{l_y l_x}^\dagger b_{l_y l_x}}. \quad (3.13)$$

In the considered antiferromagnetic background the hole creation and annihilation operators are introduced as

$$h_{l_y l_x}^\dagger = \sum_{\sigma} P_{l_y l_x}^{\sigma} X_{l_y l_x}^{0 \sigma}, \quad h_{l_y l_x} = \sum_{\sigma} P_{l_y l_x}^{\sigma} X_{l_y l_x}^{\sigma 0}. \quad (3.14)$$

The Hubbard operators can be expressed via the hole creation and annihilation operators and the spin-wave operators as

$$\begin{aligned}
X_{\mathbf{M}}^{0+} &= P_{\mathbf{M}}^+ |\mathbf{M}0\rangle \langle \mathbf{M}+| + P_{\mathbf{M}}^- |\mathbf{M}0\rangle \langle \mathbf{M}-| \mathbf{M}-\rangle \langle \mathbf{M}+| \\
&= P_{\mathbf{M}}^+ h_{\mathbf{M}}^\dagger + P_{\mathbf{M}}^- h_{\mathbf{M}}^\dagger b_{\mathbf{M}}, \\
X_{\mathbf{M}}^{0-} &= P_{\mathbf{M}}^- |\mathbf{M}0\rangle \langle \mathbf{M}-| + P_{\mathbf{M}}^+ |\mathbf{M}0\rangle \langle \mathbf{M}+| \mathbf{M}+\rangle \langle \mathbf{M}-| \\
&= P_{\mathbf{M}}^- h_{\mathbf{M}}^\dagger + P_{\mathbf{M}}^+ h_{\mathbf{M}}^\dagger b_{\mathbf{M}}.
\end{aligned} \tag{3.15}$$

Using Eqs. (3.13) and (3.15) we can rewrite the first and second sums in Hamiltonian (3.11) as

$$\sum_{\sigma} X_{\mathbf{M}_1}^{\sigma 0} X_{\mathbf{M}_2}^{0\sigma} = h_{\mathbf{M}_1} h_{\mathbf{M}_2}^\dagger b_{\mathbf{M}_2} + b_{\mathbf{M}_1}^\dagger h_{\mathbf{M}_1} h_{\mathbf{M}_2}^\dagger.$$

The spin wave operators $b_{\mathbf{M}}^\dagger, b_{\mathbf{M}}$ and the hole creation and annihilation operators $h_{\mathbf{M}}^\dagger, h_{\mathbf{M}}$, which belong to the same lattice, generally speaking, do not commute. However, in the case of low hole doping this noncommutivity can be neglected due to small densities of holes and magnons. This conclusion is also supported by calculations carried out for the unbounded lattice [45, 50, 52, 53], which demonstrated good agreement between results obtained in the spin-wave approximation and by exact diagonalization. As a result the sum $\sum_{\sigma} X_{\mathbf{M}_1}^{\sigma 0} X_{\mathbf{M}_2}^{0\sigma}$ can be approximately rewritten as

$$\sum_{\sigma} X_{\mathbf{M}_1}^{\sigma 0} X_{\mathbf{M}_2}^{0\sigma} = h_{\mathbf{M}_1} h_{\mathbf{M}_2}^\dagger (b_{\mathbf{M}_2} + b_{\mathbf{M}_1}^\dagger).$$

Substituting Eqs. (3.12), (3.13) and (3.15) into Hamiltonian (3.11) and leaving terms up to the second order in the spin-wave operators we find the Hamiltonian of the t - J model in the spin-wave approximation

$$\begin{aligned}
H_{tJ} &= t \sum_{l_y \delta} \sum_{l_x \geq 0} h_{l_y + \delta, l_x} h_{l_y l_x}^\dagger (b_{l_y l_x} + b_{l_y + \delta, l_x}^\dagger) \\
&+ t \sum_{l_y, l_x \geq 0} \left[h_{l_y, l_x + 1} h_{l_y l_x}^\dagger (b_{l_y l_x} + b_{l_y, l_x + 1}^\dagger) \right. \\
&+ \left. h_{l_y l_x} h_{l_y, l_x + 1}^\dagger (b_{l_y, l_x + 1} + b_{l_y l_x}^\dagger) \right] + H_{AF} \\
&- \frac{J}{4} \sum_{l_y, l_x \geq 0} (\nu_{l_y + 1, l_x} \nu_{l_y l_x} + \nu_{l_y, l_x + 1} \nu_{l_y l_x}) \\
&- \frac{J}{2} \sum_{l_y} \nu_{l_y 0} + \mu \sum_{l_y, l_x \geq 0} \nu_{l_y l_x},
\end{aligned} \tag{3.16}$$

where $\nu_{l_y l_x} = h_{l_y l_x}^\dagger h_{l_y l_x}$ and

$$\begin{aligned}
H_{AF} &= 2J \sum_{l_y, l_x \geq 0} \left(1 - \frac{1}{4} \delta_{l_x 0}\right) b_{l_y l_x}^\dagger b_{l_y l_x} \\
&+ \frac{J}{2} \sum_{l_y, l_x \geq 0} \left(b_{l_y+1, l_x} b_{l_y l_x} + b_{l_y+1, l_x}^\dagger b_{l_y l_x}^\dagger\right) \\
&+ \frac{J}{2} \sum_{l_y, l_x \geq 0} \left(b_{l_y, l_x+1} b_{l_y l_x} + b_{l_y, l_x+1}^\dagger b_{l_y l_x}^\dagger\right)
\end{aligned} \tag{3.17}$$

is the Hamiltonian of the 2D semi-infinite Heisenberg antiferromagnet in the spin-wave approximation. In Eq. (3.16), some constant terms were omitted and the term $2J$ was added to the chemical potential μ .

The next to the last term in the right-hand side of Hamiltonian (3.16) describes an attraction of a hole to the boundary. It originates from terms of Hamiltonian (3.11) which contain z components of spin and occupation numbers on neighboring sites. In the antiferromagnetic state, these terms give the energy gain equal to $J/2$ for each nearest-neighbour bond. In the 2D case a hole destroys 4 such bonds deep inside the crystal and only 3 bonds at the boundary. Thus, for an immobile hole it is energetically more favourable to reside at the boundary.

Considering the case of a low hole doping, in Hamiltonian (3.16) we neglect terms containing two hole occupations operators on neighboring sites.

Let us take into account the translational invariance of Hamiltonian (3.16) along the Y axis and apply the Fourier transformation

$$b_{k_y l_x} = \frac{1}{\sqrt{N_y}} \sum_{l_y} e^{ik_y l_y} b_{l_y l_x}, \quad h_{k_y l_x} = \frac{1}{\sqrt{N_y}} \sum_{l_y} e^{ik_y l_y} h_{l_y l_x}, \tag{3.18}$$

where N_y is the number of sites in the Y direction and k_y is the 1D wave vector.

Finally the Hamiltonian of the t - J model on a semi-infinite 2D lattice reads

$$\begin{aligned}
H &= H_{int} + H_{AF} + \sum_{k_y, l_x \geq 0} \mu'_{l_x} \nu_{k_y l_x}, \quad \mu'_{l_x} = \mu - \frac{J}{2} \delta_{l_x 0}, \\
H_{AF} &= 2J \sum_{k_y, l_x \geq 0} \left(1 - \frac{1}{4} \delta_{l_x 0}\right) b_{k_y l_x}^\dagger b_{k_y l_x} \\
&+ J \sum_{k_y, l_x \geq 0} \left(b_{k_y l_x} b_{-k_y, l_x+1} + b_{k_y l_x}^\dagger b_{-k_y, l_x+1}^\dagger\right) \\
&+ J \sum_{k_y, l_x \geq 0} \cos(k_y) \left(b_{k_y l_x} b_{-k_y, l_x} + b_{k_y l_x}^\dagger b_{-k_y, l_x}^\dagger\right),
\end{aligned}$$

$$\begin{aligned}
H_{int} &= N_y^{-\frac{1}{2}} \sum_{k_y k'_y} \sum_{l_x \geq 0} \sum_{s=-1}^1 \theta(l_x + s) h_{k_y, l_x + s} h_{k_y + k'_y, l_x}^\dagger \\
&\times \left(b_{k'_y, l_x} g_{k'_y s} + b_{-k_y, l_x + s}^\dagger g_{k_y + k'_y, s} \right), \tag{3.19}
\end{aligned}$$

with the interaction constant,

$$g_{k_y s} = \begin{cases} 2t \cos(k_y), & \text{if } s = 0; \\ t, & \text{if } s = \pm 1. \end{cases}$$

Refusing the constraint $l_x \geq 0$ Hamiltonian (3.19) is reduced to the spin-wave Hamiltonian on an unbounded lattice (2.17), used in Refs. [45, 50] and in a lot of subsequent works.

Analogous transformations can be carried out for a three-dimensional semi-infinite crystal [54].

4 Magnetic excitations and correlations: a semi-infinite 2D/3D lattice

4.1 The Hamiltonian

In the case of small hole concentrations we can neglect the influence of holes on the magnon Green's function and use its value for the undoped case. In addition to the 2D antiferromagnet we shall consider also the 3D antiferromagnet in order to investigate the influence of the dimensionality on the near-boundary phenomena in the magnon spectrum and nearest-neighbor spin correlations. Since the Heisenberg Hamiltonian for the 2D semi-infinite square lattice was derived in the previous chapter, in this subsection we shall concentrate our attention on a 3D simple cubic lattice. A semi-infinite 3D antiferromagnet is located in the half-space $l_x \geq 0$. An antiferromagnet is described by the Heisenberg Hamiltonian (2.14)

$$H = \frac{J}{2} \sum_{\mathbf{l}\mathbf{a}} \sum_{l_x \geq 0} \mathbf{S}_{\mathbf{l}+\mathbf{a},l_x} \mathbf{S}_{\mathbf{l},l_x} + J \sum_{l_x \geq 0} \mathbf{S}_{\mathbf{l},l_x+1} \mathbf{S}_{\mathbf{l},l_x}. \quad (4.1)$$

In the 3D case the following notations are used: sites of a simple cubic lattice are labeled by the three coordinates l_x, l_y, l_z , $\mathbf{l} = (l_y, l_z)$, and $\mathbf{a} = (\pm 1, 0), (0, \pm 1)$ are four unit vectors, which connect nearest neighbor sites in the YZ plane.

Since for low temperatures the system has the long-range antiferromagnetic ordering, its low-lying elementary excitations can be described in the spin wave approximation, which can be introduced using the Holstein-Primakoff transformation [51]:

$$\begin{aligned} S_{\mathbf{L}}^+ &= P_{\mathbf{L}}^+ \varphi_{\mathbf{L}} b_{\mathbf{L}} + P_{\mathbf{L}}^- b_{\mathbf{L}}^\dagger \varphi_{\mathbf{L}}, & S_{\mathbf{L}}^- &= P_{\mathbf{L}}^- \varphi_{\mathbf{L}} b_{\mathbf{L}} + P_{\mathbf{L}}^+ b_{\mathbf{L}}^\dagger \varphi_{\mathbf{L}}, \\ S_{\mathbf{L}}^z &= e^{i\mathbf{\Pi}\mathbf{L}} \left(\frac{1}{2} - b_{\mathbf{L}}^\dagger b_{\mathbf{L}} \right). \end{aligned} \quad (4.2)$$

Here the spin-wave operators $b_{\mathbf{L}}$ and $b_{\mathbf{L}}^\dagger$ satisfy the Boson commutation relations and

$$P_{\mathbf{L}}^\pm = \frac{1}{2} (1 \pm e^{i\mathbf{\Pi}\mathbf{L}}), \quad \mathbf{L} = (\mathbf{l}, l_x),$$

where $\mathbf{\Pi} = (\pi, \pi, \pi)$. Substituting Eq. (4.2) into Hamiltonian (4.1), dropping constant terms and terms containing more than two spin-wave operators $b_{\mathbf{L}}$,

$b_{\mathbf{L}}^\dagger$, we obtain

$$\begin{aligned}
H &= 3J \sum_{l_x \geq 0} \left(1 - \frac{1}{6} \delta_{l_x, 0}\right) b_{l_x}^\dagger b_{l_x} + \frac{J}{4} \sum_{\mathbf{1a}} \sum_{l_x \geq 0} \left(b_{\mathbf{1+a}, l_x} b_{l_x} + b_{\mathbf{1+a}, l_x}^\dagger b_{l_x}^\dagger\right) \\
&+ \frac{J}{2} \sum_{l_x \geq 0} \left(b_{\mathbf{1}, l_x+1} b_{l_x} + b_{\mathbf{1}, l_x+1}^\dagger b_{l_x}^\dagger\right). \tag{4.3}
\end{aligned}$$

Taking into account the translational invariance of Hamiltonian (4.3) in the plane YZ we use the Fourier transformation

$$b_{\mathbf{k}l_x} = \frac{1}{\sqrt{N}} \sum_{\mathbf{1}} e^{i\mathbf{k}\mathbf{1}} b_{l_x}, \tag{4.4}$$

where N is the number of sites in the periodic YZ plane and $\mathbf{k} = (k_y, k_z)$ is a 2D wave vector. After the Fourier transformation (4.4) the Hamiltonian is expressed in the following form:

$$\begin{aligned}
H &= dJ \sum_{\mathbf{k}l_x \geq 0} \left(1 - \frac{1}{z} \delta_{l_x, 0}\right) b_{\mathbf{k}l_x}^\dagger b_{\mathbf{k}l_x} + J \sum_{\mathbf{k}l_x \geq 0} \gamma_{\mathbf{k}}^{(d-1)} \left(b_{\mathbf{k}l_x} b_{-\mathbf{k}, l_x} + b_{\mathbf{k}l_x}^\dagger b_{-\mathbf{k}, l_x}^\dagger\right) \\
&+ \frac{J}{2} \sum_{\mathbf{k}l_x \geq 0} \left(b_{\mathbf{k}l_x} b_{-\mathbf{k}, l_x+1} + b_{\mathbf{k}l_x}^\dagger b_{-\mathbf{k}, l_x+1}^\dagger\right). \tag{4.5}
\end{aligned}$$

In Eq. (4.5) we combined Hamiltonians for the two and three dimensions [see Eq. (3.19)]. Here $d = 2$ or 3 is the dimensionality of the lattice and

$$\gamma_{\mathbf{k}}^{(2)} = \frac{1}{2} [\cos(k_y) + \cos(k_z)], \quad \gamma_{k_y}^{(1)} = \frac{1}{2} \cos(k_y).$$

In the 2D case \mathbf{k} reduces to k_y . It is worth noting that Hamiltonian (4.5) without the term proportional to $\delta_{l_x, 0}$ is easily diagonalized by the use of the Bogoliubov-Tyablikov transformation [51].

4.2 The magnon Green's function and its equation of motion

To investigate the magnon spectrum we introduce the two-component operator

$$\hat{B}_{\mathbf{k}l_x} = \begin{pmatrix} b_{\mathbf{k}l_x} \\ b_{-\mathbf{k}, l_x}^\dagger \end{pmatrix} \tag{4.6}$$

and define the matrix retarded Green's function (2.1)

$$\hat{D}(\mathbf{k}t l_x l'_x) = \left\langle \left\langle \hat{B}_{\mathbf{k}l_x} | \hat{B}_{\mathbf{k}'l'_x}^\dagger \right\rangle \right\rangle_t = -i\theta(t) \left\langle \left[\hat{B}_{\mathbf{k}l_x}(t), \hat{B}_{\mathbf{k}'l'_x}^\dagger \right] \right\rangle, \tag{4.7}$$

with the time dependence and the averaging determined by Eq. (4.5).

Instead of the diagonalization of Hamiltonian (4.5), it is more convenient to solve the equation of motion (2.2) for the magnon Green's function (4.7). This equation reads

$$i \frac{d}{dt} \hat{D}(\mathbf{k}t l_x l'_x) = \delta(t) \left[\hat{B}_{\mathbf{k}l_x}, \hat{B}_{\mathbf{k}l'_x}^\dagger \right] + \left\langle \left\langle \left[\hat{B}_{\mathbf{k}l_x}, H \right] \hat{B}_{\mathbf{k}l'_x}^\dagger \right\rangle \right\rangle_t. \quad (4.8)$$

The commutators $[\hat{B}_{\mathbf{k}l_x}, H]$ are calculated using the commutation relations for the spin-wave operators $b_{\mathbf{k}l_x}, b_{\mathbf{k}l_x}^\dagger$,

$$\begin{aligned} [b_{\mathbf{k}l_x}, H] &= dJ \left(1 - \frac{1}{z} \delta_{l_x,0} \right) b_{\mathbf{k}l_x} + 2J\gamma_{\mathbf{k}}^{(d-1)} b_{-\mathbf{k},l_x}^\dagger \\ &\quad + \frac{J}{2} \left[b_{-\mathbf{k},l_x+1}^\dagger + b_{-\mathbf{k},l_x-1}^\dagger \right], \\ [b_{-\mathbf{k},l_x}^\dagger, H] &= -dJ \left(1 - \frac{1}{z} \delta_{l_x,0} \right) b_{-\mathbf{k},l_x}^\dagger - 2J\gamma_{\mathbf{k}}^{(d-1)} b_{\mathbf{k}l_x} \\ &\quad - \frac{J}{2} \left[b_{\mathbf{k},l_x+1} + b_{\mathbf{k},l_x-1} \right]. \end{aligned} \quad (4.9)$$

Substituting commutators from (4.9) into the equation of motion (4.8), we obtain

$$\begin{aligned} i \frac{d}{dt} \hat{D}(\mathbf{k}t l_x l'_x) &= \delta(t) \delta_{l_x l'_x} \hat{\tau}_3 + J \left[d \left(1 - \frac{1}{z} \delta_{l_x,0} \right) \hat{\tau}_3 + 2\gamma_{\mathbf{k}}^{(d-1)} \hat{\tau}_1 \right] \hat{D}(\mathbf{k}t l_x l'_x) \\ &\quad + \frac{J}{2} \hat{\tau}_1 \left[\hat{D}(\mathbf{k}t, l_x + 1, l'_x) + \hat{D}(\mathbf{k}t, l_x - 1, l'_x) \right], \end{aligned} \quad (4.10)$$

where the matrices $\hat{\tau}_1$ and $\hat{\tau}_3$ are given by

$$\hat{\tau}_1 = \begin{pmatrix} 0 & 1 \\ -1 & 0 \end{pmatrix}, \quad \hat{\tau}_3 = \begin{pmatrix} 1 & 0 \\ 0 & -1 \end{pmatrix}.$$

To solve the equation of motion (4.10) we use a modification of the method applied by I. M. Lifshits for the problem of a local defect [8–10]. In this method, the magnon Green's function $\hat{D}(\mathbf{k}t l_x l'_x)$ is expressed in terms of Green's function $\hat{D}^{(0)}(\mathbf{k}t l_x l'_x)$ of a simpler problem which is described by Hamiltonian (4.5) without the term proportional to $\delta_{l_x,0}$. This latter Hamiltonian can be easily diagonalized by the use of Bogoliubov-Tyablikov transformation [51]. The solution of the equation of motion (4.10) can be written as

$$\hat{D}(\mathbf{k}t l_x l'_x) = \hat{D}^{(0)}(\mathbf{k}t l_x l'_x) - \frac{J}{2} \int_{-\infty}^{\infty} dt' \hat{D}^{(0)}(\mathbf{k}, t - t', l_x, 0) \hat{D}(\mathbf{k}t' 0 l'_x). \quad (4.11)$$

In order to make certain that Eq. (4.11) is indeed the solution of Eq. (4.10) it is necessary to substitute the former equation into the latter and use the

equation of motion for $\hat{D}^{(0)}(\mathbf{k}l_x l'_x)$. This equation coincides with Eq. (4.10) without the term proportional to $\delta_{l_x 0}$.

It is worth mentioning that except for the matrix form and the dependence on \mathbf{k} the equation of motion (4.11) is similar in form to the equation for Green's function of a crystal with a local defect [8–10]. After Fourier transformation (2.3), the use of the convolution theorem for the Fourier transform [55] and some mathematical manipulations we obtain the expression for the magnon Green's function

$$\begin{aligned} \hat{D}(\mathbf{k}\omega l_x l'_x) &= \hat{D}^{(0)}(\mathbf{k}\omega l_x l'_x) \\ &- \frac{J}{2} \hat{D}^{(0)}(\mathbf{k}\omega l_x 0) \left[\hat{\tau}_0 + \frac{J}{2} \hat{D}^{(0)}(\mathbf{k}\omega 00) \right]^{-1} \hat{D}^{(0)}(\mathbf{k}\omega 0 l'_x), \end{aligned} \quad (4.12)$$

where $\hat{\tau}_0$ is the 2×2 unit matrix.

4.3 The magnon Green's function $\hat{D}^{(0)}$

To calculate the magnon Green's function $\hat{D}^{(0)}(\mathbf{k}\omega l_x l'_x)$ it is necessary to diagonalize Hamiltonian (4.5) without the term proportional to $\delta_{l_x 0}$. This can be fulfilled using the Bogoliubov-Tyablikov transformation [51],

$$b_{\mathbf{k}l_x} = \sum_{k_x} \left(u_{\mathbf{k}l_x k_x} \beta_{\mathbf{k}k_x} + v_{\mathbf{k}l_x k_x} \beta_{-\mathbf{k}, k_x}^\dagger \right). \quad (4.13)$$

In the new representation Hamiltonian (4.5) has the diagonal form,

$$H' = \sum_{\mathbf{k}k_x} E_{\mathbf{k}k_x} \beta_{\mathbf{k}k_x}^\dagger \beta_{\mathbf{k}k_x} + \text{const.}$$

The transformation which is opposite to Eq. (4.13) reads

$$\beta_{\mathbf{k}k_x} = \sum_{l_x \geq 0} \left(u_{\mathbf{k}l_x k_x}^* b_{\mathbf{k}l_x} - v_{-\mathbf{k}, l_x k_x} b_{-\mathbf{k}, l_x}^\dagger \right). \quad (4.14)$$

Since new operators $\beta_{\mathbf{k}i}, \beta_{\mathbf{k}i}^\dagger$ satisfy the Boson commutation relations, the following conditions are imposed on the coefficients $u_{\mathbf{k}l_x k_x}$ and $v_{\mathbf{k}l_x k_x}$:

$$\begin{aligned} \sum_{k_x} \left(u_{\mathbf{k}l_x k_x} u_{\mathbf{k}l'_x k_x}^* - v_{\mathbf{k}l_x k_x} v_{\mathbf{k}l'_x k_x}^* \right) &= \delta_{l_x l'_x}, \\ \sum_{k_x} \left(u_{\mathbf{k}l_x k_x} v_{-\mathbf{k}, l'_x k_x} - v_{\mathbf{k}l_x k_x} u_{-\mathbf{k}, l'_x k_x} \right) &= 0, \\ \sum_{l_x \geq 0} \left(u_{\mathbf{k}l_x k_x} u_{\mathbf{k}l_x k'_x}^* - v_{-\mathbf{k}, l_x k'_x} v_{-\mathbf{k}, l_x k_x}^* \right) &= \delta_{k_x k'_x}, \\ \sum_{l_x \geq 0} \left(u_{-\mathbf{k}, l_x k_x}^* v_{-\mathbf{k}l_x k'_x} - v_{\mathbf{k}l_x k_x} u_{\mathbf{k}l_x k'_x}^* \right) &= 0 \end{aligned} \quad (4.15)$$

If we use Eqs. (4.5), (4.15) in the relation

$$[\beta_{\mathbf{k}k_x}, H'] = E_{\mathbf{k}k_x} \beta_{\mathbf{k}k_x} \quad (4.16)$$

we find the system of equations for the determination of the coefficients $u_{\mathbf{k}l_x k_x}$, $v_{\mathbf{k}l_x k_x}$ and the energy of magnetic excitations $E_{\mathbf{k}k_x}$,

$$\begin{aligned} E_{\mathbf{k}k_x} u_{\mathbf{k}l_x k_x}^* &= dJ u_{\mathbf{k}l_x k_x}^* + 2J \gamma_{\mathbf{k}}^{(d-1)} v_{-\mathbf{k}, l_x k_x} \\ &\quad + \frac{J}{2} [v_{-\mathbf{k}, l_x+1, k_x} + v_{-\mathbf{k}, l_x+1, k_x}] \\ -E_{\mathbf{k}k_x} v_{-\mathbf{k}, l_x k_x} &= dJ v_{-\mathbf{k}, l_x k_x} + 2J \gamma_{\mathbf{k}}^{(d-1)} u_{\mathbf{k}l_x k_x}^* \\ &\quad + \frac{J}{2} [u_{\mathbf{k}, l_x+1, k_x}^* + u_{-\mathbf{k}, l_x+1, k_x}^*], \end{aligned} \quad (4.17)$$

with the boundary conditions

$$u_{\mathbf{k}, l_x=-1, k_x}^* = 0, \quad v_{-\mathbf{k}, l_x=-1, k_x} = 0. \quad (4.18)$$

The solutions for this system of equations can be written in the form

$$u_{\mathbf{k}l_x k_x}^* = A_{\mathbf{k}k_x} e^{\varkappa_{k_x} l_x}, \quad v_{-\mathbf{k}, l_x k_x} = B_{\mathbf{k}k_x} e^{\varkappa_{k_x} l_x}, \quad (4.19)$$

where \varkappa_{k_x} is in general a complex number. Due to the linearity of system (4.17) a linear combination of such solutions which correspond to the same energy $E_{\mathbf{k}k_x}$ is also a solution of system (4.17). Substituting solution (4.19) into system (4.17) we obtain a system of two equations for the coefficients $A_{\mathbf{k}k_x}, B_{\mathbf{k}k_x}$

$$\begin{aligned} (dJ - E_{\mathbf{k}k_x}) A_{\mathbf{k}k_x} + J [2\gamma_{\mathbf{k}}^{(d-1)} + \cosh(\varkappa_{k_x})] B_{\mathbf{k}k_x} &= 0 \\ J [2\gamma_{\mathbf{k}}^{(d-1)} + \cosh(\varkappa_{k_x})] A_{\mathbf{k}k_x} + (dJ + E_{\mathbf{k}k_x}) B_{\mathbf{k}k_x} &= 0 \end{aligned} \quad (4.20)$$

instead of the infinite system of equations (4.17). The existence condition of non-trivial solutions of system (4.20) gives the energy of magnetic excitations,

$$E_{\mathbf{k}k_x} = J \sqrt{d^2 - [2\gamma_{\mathbf{k}}^{(d-1)} + \cosh(\varkappa_{k_x})]^2}. \quad (4.21)$$

Since the energy $E_{\mathbf{k}k_x}$ has to be a real number, the imaginary part of $\cosh(\varkappa_{k_x})$ should be zero,

$$\text{Im}[\cosh(\varkappa_{k_x})] = -\sinh[\text{Re}(\varkappa_{k_x})] \sin[\text{Im}(\varkappa_{k_x})] = 0.$$

From this condition it follows that \varkappa_{k_x} has to be either real or purely imaginary. Solutions with real \varkappa_{k_x} or their linear combination either do not satisfy boundary conditions (4.18) or grow unrestrictedly deep into the crystal, in

contradiction with conditions (4.15). These solutions cannot be admixed to solutions with imaginary \varkappa_{k_x} , since these two groups of solutions correspond to different energy ranges for a fixed \mathbf{k} (the energies are equal only for $\varkappa_{k_x} = 0$, which corresponds to solutions independent of the coordinate l_x and therefore, unsatisfying the boundary conditions). Only linear combinations of solutions with imaginary and opposite in sign \varkappa_{k_x} , $\varkappa_{k_x} = \pm ik_x$, the standing waves, satisfy conditions (4.15) and (4.18). These solutions read

$$u_{\mathbf{k}l_x k_x}^* = A_{\mathbf{k}k_x} \sin[k_x(l_x + 1)], \quad v_{-\mathbf{k}, l_x k_x} = B_{\mathbf{k}k_x} \sin[k_x(l_x + 1)], \quad (4.22)$$

where k_x varies continuously in the range $(0, \pi)$. Thus, in Eqs. (4.13)-(4.15) sums over k_x and Kronecker symbols containing k_x have to be substituted with integrals and the Dirac delta functions. One of equations of the system (4.20) and the first relation for $u_{\mathbf{k}l_x k_x}, v_{-\mathbf{k}, l_x k_x}$ in Eq. (4.15) allows us to find the coefficients $A_{\mathbf{k}k_x}, B_{\mathbf{k}k_x}$,

$$\begin{aligned} A_{\mathbf{k}k_x} &= \sqrt{\frac{2}{\pi}} \frac{dJ + E_{\mathbf{k}k_x}}{\sqrt{(dJ + E_{\mathbf{k}k_x})^2 - (dJ\gamma_{\mathbf{k}k_x}^{(d)})^2}} \\ &= \sqrt{\frac{2}{\pi}} \frac{1}{2} \left(\sqrt[4]{\frac{1 - \gamma_{\mathbf{k}k_x}^{(d)}}{1 + \gamma_{\mathbf{k}k_x}^{(d)}}} + \sqrt[4]{\frac{1 + \gamma_{\mathbf{k}k_x}^{(d)}}{1 - \gamma_{\mathbf{k}k_x}^{(d)}}} \right), \\ B_{\mathbf{k}k_x} &= -\sqrt{\frac{2}{\pi}} \frac{dJ\gamma_{\mathbf{k}k_x}^{(d)}}{\sqrt{(dJ + E_{\mathbf{k}k_x})^2 - (dJ\gamma_{\mathbf{k}k_x}^{(d)})^2}} \\ &= \sqrt{\frac{2}{\pi}} \frac{1}{2} \left(\sqrt[4]{\frac{1 - \gamma_{\mathbf{k}k_x}^{(d)}}{1 + \gamma_{\mathbf{k}k_x}^{(d)}}} - \sqrt[4]{\frac{1 + \gamma_{\mathbf{k}k_x}^{(d)}}{1 - \gamma_{\mathbf{k}k_x}^{(d)}}} \right), \\ E_{\mathbf{k}k_x} &= dJ \sqrt{1 - (\gamma_{\mathbf{k}k_x}^{(d)})^2}, \end{aligned} \quad (4.23)$$

where

$$\gamma_{\mathbf{k}k_x}^{(3)} = \frac{1}{3}[\cos(k_x) + \cos(k_y) + \cos(k_z)], \quad \gamma_{k_y k_x}^{(2)} = \frac{1}{2}[\cos(k_x) + \cos(k_y)].$$

Here we took into account the fact that quantity $A_{\mathbf{k}k_x}^2 - B_{\mathbf{k}k_x}^2$ does not depend on k_x .

With a knowledge of eigenfunctions and eigenenergies of the Hamiltonian,

the Green's functions $\hat{D}^{(0)}(\mathbf{k}\omega l_x l'_x)$ can be easily calculated

$$\begin{aligned} \hat{D}^{(0)}(\mathbf{k}\omega l_x l'_x) &= \int_0^\pi dk_x \sin[k_x(l_x + 1)] \sin[k_x(l'_x + 1)] \\ &\times \left(\frac{\hat{P}_{\mathbf{k}k_x}}{\omega - E_{\mathbf{k}k_x} + i\eta} - \frac{\hat{Q}_{\mathbf{k}k_x}}{\omega + E_{\mathbf{k}k_x} + i\eta} \right), \end{aligned} \quad (4.24)$$

$$\begin{aligned} \hat{P}_{\mathbf{k}k_x} &= \begin{pmatrix} A_{\mathbf{k}k_x}^2 & A_{\mathbf{k}k_x} B_{\mathbf{k}k_x} \\ A_{\mathbf{k}k_x} B_{\mathbf{k}k_x} & B_{\mathbf{k}k_x}^2 \end{pmatrix}, \\ \hat{Q}_{\mathbf{k}k_x} &= \begin{pmatrix} B_{\mathbf{k}k_x}^2 & A_{\mathbf{k}k_x} B_{\mathbf{k}k_x} \\ A_{\mathbf{k}k_x} B_{\mathbf{k}k_x} & A_{\mathbf{k}k_x}^2 \end{pmatrix}, \end{aligned}$$

where $\eta = +0$.

From Eqs. (4.12), (4.24) one can derive the following property of Green's function:

$$D_{ij}(\mathbf{k}\omega l_x l'_x) = D_{ji}(\mathbf{k}\omega l'_x l_x). \quad (4.25)$$

4.4 The magnon spectrum

The poles of Green's function (4.24) correspond to standing spin waves (4.22), (4.23). Apart from them, the magnon Green's function $\hat{D}(\mathbf{k}\omega l_x l'_x)$ may have poles connected with the second term in the right-hand side of Eq. (4.12). In Figs. 1-4 the imaginary part of Green's functions $\hat{D}(\mathbf{k}\omega l_x l_x)$ is shown in comparison with the Green's functions $\hat{D}^{(0)}(\mathbf{k}\omega l_x l_x)$ for various distances l_x from the edge of the 3D and 2D antiferromagnets. On the edge, $l_x = 0$, the magnon spectrum $\text{Im}\hat{D}(\mathbf{k}\omega l_x l_x)$ is dominated by the peak, which frequency coincides with the zero of the denominator of the second term in the right-hand side of Eq. (4.12) [see Figs. 1(a) and 3(a)]. This means that this peak arises from this term. As seen from Figs. 1(a) and 3(a), the standing spin waves manifest themselves as a weak shoulder on the high-frequency side of the peak. *Consequently excitations corresponding to the peak eject standing waves from the edge layer (row) of sites.* The similar situation is observed in the second layer (row). However, as seen from Figs. 1(b) and 3(b), already in the third layer (row) the mentioned peak is weak and the spectrum is dominated by the continuum of standing waves. *Thus, the boundary divides the antiferromagnet into two regions with different spin excitations.* The two layers near the edge are the location of the mode connected with the pole of the second term in the right-hand side of Eq. (4.12). This excitation can be named the near-boundary mode. Excitations of the rest of the crystal, the bulk modes, are the standing spin waves related to the first term in Eq. (4.12). This picture is in many respects similar to the situation in the above-mentioned problem of a local defect [8–10]: if local states arise near the defect, they eject bulk states from the defect region, and the crystal appears to be divided into the parts with

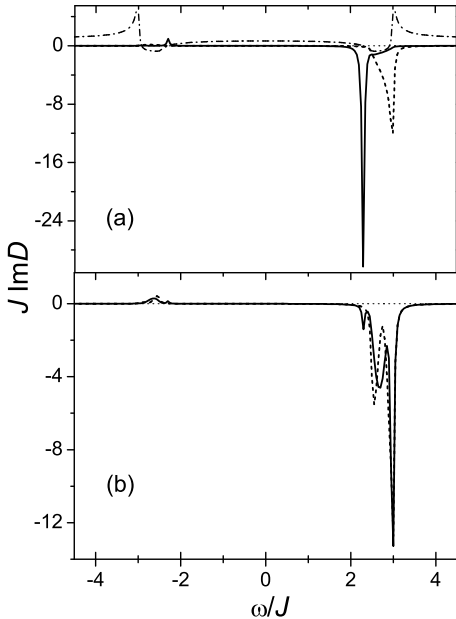


Figure 1: The 3D case. The imaginary parts of Green's functions $D_{11}(\mathbf{k}\omega l_x l_x)$ (the solid lines) and $D_{11}^{(0)}(\mathbf{k}\omega l_x l_x)$ (the dashed lines) for (a) $l_x = 0$ and (b) $l_x = 2$. $\mathbf{k} = (0, 0.6\pi)$. In part (a), the dash-dotted line demonstrates the real part of the denominator in the second term in the right-hand side of Eq. (4.12).

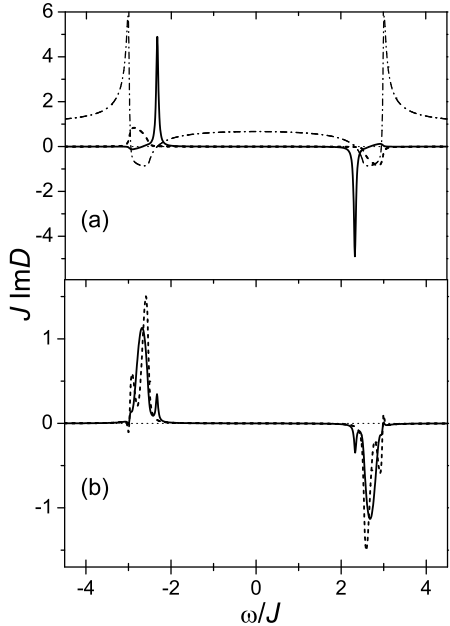


Figure 2: The same as in Fig. 1 for Green's functions $D_{12}(\mathbf{k}\omega l_x l_x)$ and $D_{12}^{(0)}(\mathbf{k}\omega l_x l_x)$.

different electronic excitations.

Figure 5 demonstrates the dispersions of the near-boundary spin waves of the 3D (a) and 2D (b) antiferromagnets derived from the Green's functions $\text{Im}D_{11}(\mathbf{k}\omega l_x l_x)$ for $l_x = 0$. In the 3D case the dispersion (the solid lines) is shown along the symmetry lines of the Brillouin zone. For the d -dimensional crystal the dispersion is described by the formula

$$\omega_{\mathbf{k}} = \sqrt{d(d-1)}J\sqrt{1 - \left(\gamma_{\mathbf{k}}^{(d-1)}\right)^2}. \quad (4.26)$$

This formula resembles the dispersion of the spin waves in the $(d-1)$ -dimensional unbounded crystal [47] [see also Eq. (4.23)],

$$\omega_{\mathbf{k}} = (d-1)J\sqrt{1 - \left(\gamma_{\mathbf{k}}^{(d-1)}\right)^2}. \quad (4.27)$$

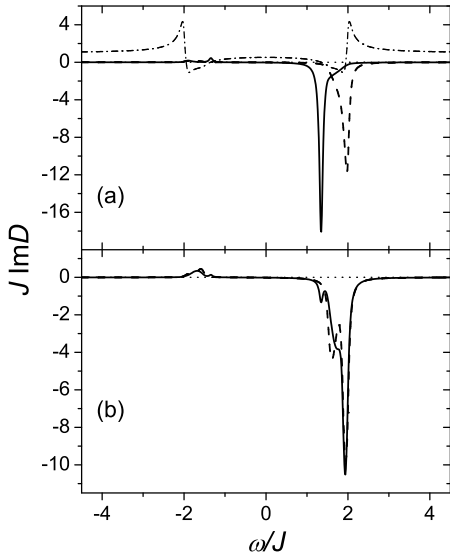


Figure 3: The 2D case. The imaginary parts of Green's functions $D_{11}(k_y\omega l_x l_x)$ (the solid lines) and $D_{11}^{(0)}(k_y\omega l_x l_x)$ (the dashed lines) for (a) $l_x = 0$ and (b) $l_x = 2$. $k_y = 0.6\pi$. In part (a), the dash-dotted line demonstrates the real part of the denominator in the second term in the right-hand side of Eq. (4.12).

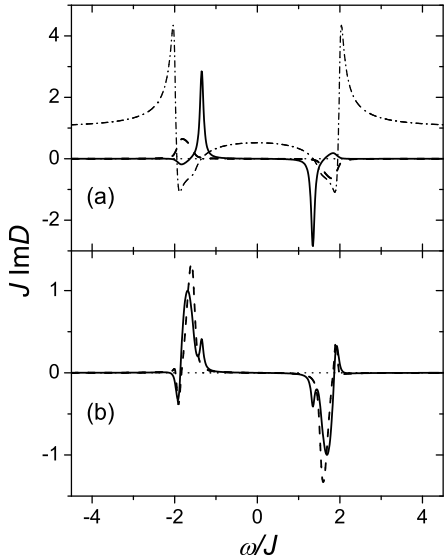


Figure 4: The same as in Fig. 3 for Green's functions $D_{12}(k_y\omega l_x l_x)$ and $D_{12}^{(0)}(k_y\omega l_x l_x)$.

This dispersion for $d = 3$ and 2 is shown with the dashed lines in Fig. 5. Thus, the near-boundary mode has dimensionality one less than that of the bulk mode. As seen from comparison of Eqs. (4.26), (4.27) and from Fig. 5, the near-boundary mode has somewhat increased frequency in comparison with the $(d - 1)$ -dimensional magnon mode. Notice that near $\mathbf{k} = (0, 0)$ and $\mathbf{k} = (\pi, \pi)$ in the 3D case and near $k_y = 0$ and $k_y = \pi$ in the 2D case the near-boundary mode is ill-defined, since the real part of the denominator of the second term in the right-hand side of Eq. (4.12) is small but non-zero.

4.5 Spin correlations

The nearest-neighbor spin correlations can be expressed via the spin-wave operators (4.2) with the use of the translational invariance of Hamiltonian (4.4) as

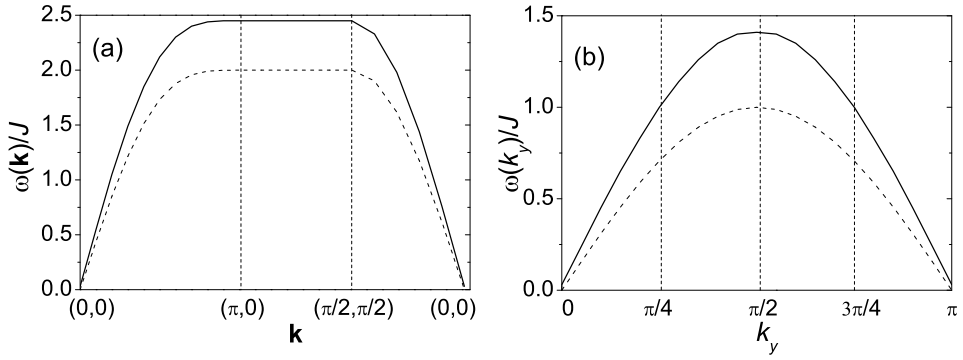


Figure 5: The dispersion of the near-boundary modes in the 3D (a) and 2D (b) cases (the solid lines). The dashed lines demonstrate the dispersions of the spin waves in the unbounded 2D (a) and 1D (b) crystals, Eq. (4.27).

$$\begin{aligned}
\langle \mathbf{S}_L \mathbf{S}_{L'} \rangle &= \frac{1}{2N} \sum_{\mathbf{k}} \left\{ 2 \cos[\mathbf{k}(1 - 1')] \langle b_{\mathbf{k}l_x} b_{-\mathbf{k},l'_x} \rangle + \langle b_{\mathbf{k}l_x}^\dagger b_{\mathbf{k}l_x} \rangle \right. \\
&\quad \left. + \langle b_{\mathbf{k}l'_x}^\dagger b_{\mathbf{k}l'_x} \rangle \right\} - \frac{1}{4}.
\end{aligned} \tag{4.28}$$

The correlation functions in Eq. (4.28) are connected with magnon Green's function (4.12) by the relation (see Appendix)

$$\langle \hat{B}_{\mathbf{k}l_x} \hat{B}_{\mathbf{k}l'_x}^\dagger \rangle = \int_{-\infty}^{\infty} \frac{d\omega}{\pi} \frac{\text{Im}[\hat{D}(\mathbf{k}\omega l_x l'_x)]}{e^{-\omega\beta} - 1}. \tag{4.29}$$

Let us consider the nearest-neighbor spin correlations which are parallel and perpendicular to the boundary,

$$C_L = \langle \mathbf{S}_{1+\mathbf{a},l_x} \mathbf{S}_{1l_x} \rangle, \quad C_T = \langle \mathbf{S}_{1,l_x+1} \mathbf{S}_{1l_x} \rangle. \tag{4.30}$$

For $T = 0$ with the use of Eq. (4.29) these spin correlations read

$$\begin{aligned}
C_L &= -\frac{1}{N} \sum_{\mathbf{k}} \cos(k_y) \int_0^{\infty} \frac{d\omega}{\pi} \text{Im} D_{12}(\mathbf{k}\omega l_x l_x) \\
&\quad - \frac{1}{N} \sum_{\mathbf{k}} \int_0^{\infty} \frac{d\omega}{\pi} \text{Im} D_{22}(\mathbf{k}\omega l_x l_x) - \frac{1}{4},
\end{aligned}$$

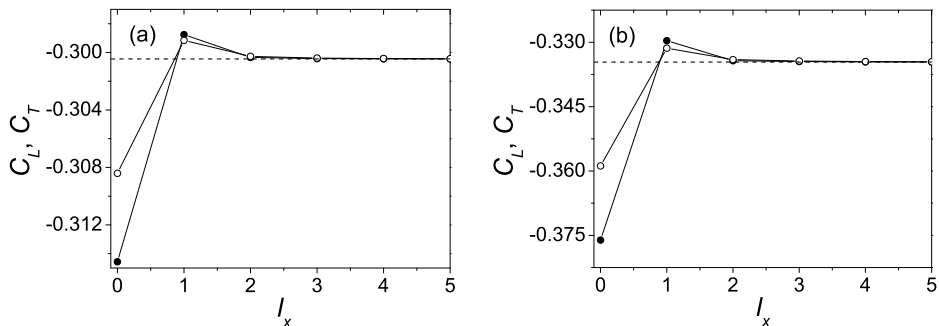


Figure 6: The nearest-neighbor spin correlations parallel (filled circles) and perpendicular (open circles) to the boundary of the 3D (a) and 2D (b) antiferromagnets as functions of the distance l_x from the boundary for $T = 0$. Solid lines are the guide to the eye. The dashed lines indicate the bulk values.

$$\begin{aligned}
C_T &= -\frac{1}{N} \sum_{\mathbf{k}} \int_0^{\infty} \frac{d\omega}{\pi} \text{Im} D_{12}(\mathbf{k}\omega l_x, l_x + 1) - \frac{1}{2N} \sum_{\mathbf{k}} \int_0^{\infty} \frac{d\omega}{\pi} \text{Im} D_{22}(\mathbf{k}\omega l_x l_x) \\
&- \frac{1}{2N} \sum_{\mathbf{k}} \int_0^{\infty} \frac{d\omega}{\pi} \text{Im} D_{22}(\mathbf{k}\omega, l_x + 1, l_x + 1) - \frac{1}{4}.
\end{aligned} \tag{4.31}$$

The calculated values of these spin correlations are shown in Fig. 6 for 3D (a) and 2D (b) antiferromagnets. As seen from the figure, the main deviations from the bulk value of the correlations fall on the boundary and the second to the boundary layers (rows), i.e. on the existence domain of the near-boundary mode. The largest in absolute value spin correlations account for the boundary where Green's function is dominated by the near-boundary mode. As was shown above, this mode has dimensionality one less than that of the bulk excitations. Notice that moduli of nearest-neighbor spin correlations in unbounded crystals decrease monotonously with the growth of the crystal dimensionality. In accord with our calculations these moduli are equal to 0.3005 and 0.3346 in the 3D and 2D cases, respectively, which is in good agreement with earlier calculations [56–58]. In the one-dimensional antiferromagnet the modulus of the nearest-neighbor correlation equals to 0.4432 [47]. Thus, it is reasonable to relate the increased spin correlations near the boundary to the decreased dimensionality of the near-boundary mode in comparison with the bulk excitations. Another interpretation of this result, first observed in Monte Carlo simulations [31], was suggested in Refs. [32, 33] where it was connected with the enlarged valence-bond-solid correlations near the edge. The correlations in the second row and between the second and third rows are smaller than in the bulk due to the destructive summation of the contributions of near-boundary and bulk excitations. [see Eq. (4.12)]. Already in the third layer from the boundary the correlations differ only slightly from the bulk value. Near the boundary the

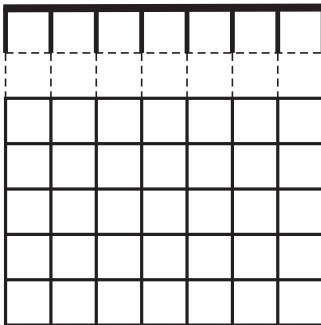


Figure 7: The pattern of nearest-neighbor spin correlations near the boundary of the 3D or 2D antiferromagnet. Thin solid lines indicate spin correlations approximately equal to the bulk value, thick solid lines are correlations larger in absolute value, while dotted lines correspond to correlations smaller than the bulk value.

pattern of spin correlations resembles the comb structure [31] shown in Fig. 7.

From Fig. 6 it can be seen that qualitative dependencies of spin correlations on the distance from the boundary are similar for the 3D and 2D cases. However, there is a quantitative difference (see Fig. 8). In the 2D case the deviations from the bulk value are greater than in the 3D case – in the former case the largest deviation is equal to 12% in comparison with 5% in the latter.

As mentioned above, the strengthening of spin correlations near the boundary of 2D clusters was first observed in Monte Carlo simulations [31]. If results in Fig. 6 are compared with the data of these simulations two differences stand out:

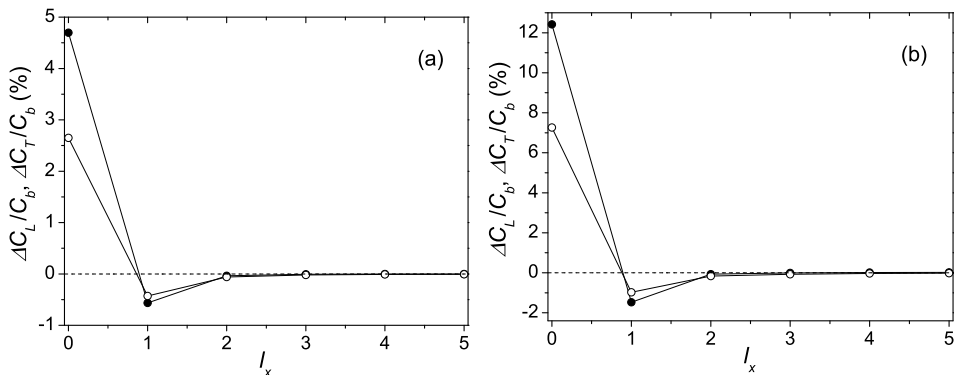


Figure 8: Deviations $\Delta C_{L,T} = C_{L,T} - C_b$ of the nearest-neighbor spin correlations from the bulk value C_b parallel (filled circles) and perpendicular (open circles) to the boundary of the 3D (a) and 2D (b) antiferromagnets as functions of the distance l_x from the boundary for $T = 0$. Solid lines are the guide to the eye.

- i) In our calculations, the absolute value of the edge correlation on the parallel bond is larger than on the bond perpendicular to the edge, while in the Monte Carlo data the relation is opposite.
- ii) In the Monte Carlo data there are weak oscillations of spin correlations around the bulk value which are perceptible over a few lattice periods from the edge, while such oscillations are missing from our results.

Partly, these differences can be ascribed to the dissimilarity of the used samples – a square-shaped finite crystal in the Monte Carlo simulations and a semi-infinite crystal in our case. However, we suppose that the main reason for these differences is the quasi-1D character of the boundary mode because this mode is the origin of the mentioned peculiarities. However, as known, the spin-wave approximation is unsuitable for the 1D antiferromagnet. Therefore, it is believed that the used approach gives only a rough description of the boundary excitations. It would be interesting to compare our results [54, 59] for the 3D case, when both the boundary and bulk modes are satisfactorily described by the spin-wave approximation, with Monte Carlo data. However, to our knowledge such simulations are lacking.

5 Hole excitations: a semi-infinite 2D lattice

5.1 The Dyson equation

Now let us turn to the calculation of the hole Green's function in the 2D t - J model on a semi-infinite lattice,

$$G(k_y \tau l_x l'_x) = -\langle \mathcal{T} h_{k_y l_x}(\tau) h_{k_y l'_x}^\dagger \rangle. \quad (5.1)$$

We use the Matsubara Green's function to apply the perturbation theory for its calculation. In this chapter the case of small hole concentrations is considered. As mentioned above, in this case the undoped magnon Green's function considered in the previous chapter can be used in the calculations. Its Matsubara counterpart reads

$$\hat{D}(k_y \tau l_x l'_x) = -\langle \mathcal{T} \hat{B}_{k_y l_x}(\tau) \hat{B}_{k_y l'_x}^\dagger \rangle, \quad (5.2)$$

and the Fourier transform will be labeled by the Boson Matsubara frequency ω_ν .

We use the perturbation theory with the expansion in powers of the hole-magnon interaction H_{int} (3.19), in full analogy with earlier works carried for an unbounded lattice [45, 50]. For this latter case, the self-energy equation (the Dyson equation) was obtained in the non-crossing approximation in which diagrams with intersecting magnon lines were neglected. It was shown that results obtained in this approximation are in good agreement with data of exact diagonalization. Therefore we also use this approximation for a semi-infinite lattice.

Within the perturbation theory (see Eq. (2.8)) the Matsubara Green's function (5.1) reads

$$\begin{aligned} G(k_y \tau l_x l'_x) &= -\sum_{n=0}^{\infty} \frac{(-1)^n}{n!} \int_0^\beta \cdots \int_0^\beta d\tau_1 \cdots d\tau_n \\ &\times \langle \mathcal{T} h_{k_y l_x}(\tau) h_{k_y l'_x}^\dagger \tilde{H}_{int}(\tau_1) \cdots \tilde{H}_{int}(\tau_n) \rangle_{0,c}, \end{aligned} \quad (5.3)$$

where averaging and time dependencies of operators are determined with the non-interacting Hamiltonian

$$H_0 = H_{AF} + \sum_{k_y l_x \geq 0} \mu'_{l_x} \nu_{k_y l_x}.$$

In the non-crossing approximation one can obtain the following self-energy equation (2.10) for the Fourier transform (2.9) of the hole Matsubara Green's

function (5.1):

$$\begin{aligned}
G(k_y n l_x l'_x) &= \sum_{l_{x1}, l_{x2} \geq 0} G^{(0)}(k_y n l_x l_{x1}) \Sigma_{sun}(k_y n l_{x1} l_{x2}) G(k_y n l_{x2} l'_x) \\
&+ \sum_{l_{x1}} \sum_{s=-1}^1 G^{(0)}(k_y n l_x l_{x1}) \Sigma_{bub}(k_y n l_{x1} s) G(k_y n, l_{x1} + s, l'_x) \\
&+ G^{(0)}(k_y n l_x l'_x), \tag{5.4}
\end{aligned}$$

$$\begin{aligned}
\Sigma_{sun}(k_y n l_x l'_x) &= -\frac{T}{N_y} \sum_{k'_y, \nu} \sum_{s, s'=-1}^1 G(k_y - k'_y, n - \nu, l_x + s, l'_x + s') \\
&\times \theta(l_x + s) \theta(l'_x + s') [g_{k_y - k'_y, s} g_{k_y s'} D_{12}(k'_y \nu l_x, l'_x + s') \\
&+ g_{k_y - k'_y, s} g_{k_y - k'_y, s'} D_{11}(k'_y \nu l_x l'_x) \\
&+ g_{k_y s} g_{k_y s'} D_{22}(k'_y \nu, l_x + s, l'_x + s') \\
&+ g_{k_y s} g_{k_y - k'_y, s'} D_{21}(k'_y \nu, l_x + s, l'_x)], \tag{5.5}
\end{aligned}$$

$$\begin{aligned}
\Sigma_{bub}(k_y n l_x s) &= -\frac{T}{N_y} \sum_{k'_y} \sum_{l'_x \geq 0} \sum_{s'=-1}^1 \theta(l_x + s) \langle h_{k'_y, l'_x + s} h_{k'_y, l'_x}^\dagger \rangle g_{k_y s} g_{k'_y s'} \\
&\times [D_{21}(00, l_x + s, l'_x + s') + D_{22}(00, l_x + s, l'_x) \\
&+ D_{11}(00 l_x, l'_x + s') + D_{12}(00 l_x l'_x)], \tag{5.6}
\end{aligned}$$

where

$$G^{(0)}(k_y n l_x l'_x) = \frac{\delta_{l_x l'_x}}{i\omega_n - \mu'_{l_x}} \tag{5.7}$$

with μ'_{l_x} taking into account the attraction of a hole to the boundary, and $D_{ij}(k_y \nu l_x l'_x)$ (3.19) is the Fourier transform (2.9) of the components of the matrix magnon Matsubara Green's function $\hat{D}(k_y \tau l_x l'_x)$ (5.2).

In the Dyson equation (5.4), self-energies $\Sigma_{sun}(k_y n l_x l'_x)$ (5.5), $\Sigma_{bub}(k_y n l_x l'_x)$ (5.6) describe the contributions of the sunrise and bubble diagrams (see Fig. 9), respectively. In this figure, the solid and dashed lines indicate the hole and

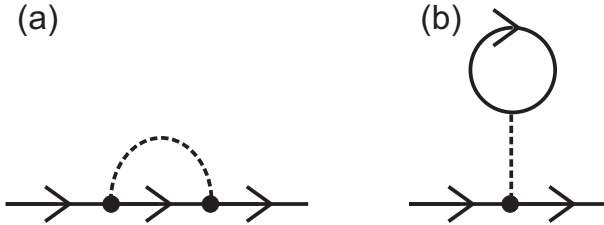


Figure 9: The sunrise (a) and bubble (b) diagrams.

the magnon Green's functions, respectively. It is worth noting that in the case

of an unbounded crystal a contribution of the bubble diagram vanishes. In a semi-infinite crystal this latter contribution is in general case nonzero and is determined by the multiplier

$$\sum_{k_y} g_{k_y s} \langle h_{k_y, l_x + s} h_{k_y l_x}^\dagger \rangle.$$

in the self-energy Σ_{bub} (5.6). In this multiplier, the mean value can be expressed through the retarded hole Green's function $G(k_y \omega l_x l'_x)$ as

$$\langle h_{k_y l_x} h_{k_y l'_x}^\dagger \rangle = - \int_{-\infty}^{\infty} \frac{d\omega}{\pi} \frac{\text{Im}G(k_y \omega l_x l'_x)}{1 + e^{-\omega/T}}.$$

For $T = 0$ the integration is carried out over the unoccupied states. For small hole concentrations these are in fact all states and therefore one can rewrite the integral as

$$- \int_{-\infty}^{\infty} \frac{d\omega}{\pi} \text{Im}G(k_y \omega l_x l'_x) = \delta_{l_x l'_x}.$$

Thus, for $s = \pm 1$ the multiplier is small because the mean value is negligible, while for $s = 0$ it is small because $g_{k_y 0} \propto \cos(k_y)$ and the sum over k_y is negligible. We conclude that in the semi-infinite crystal in the case of small hole concentrations the contribution of the bubble diagram can be also neglected, as in the unbounded crystal. The self-energy equation (5.4) can be rewritten in a simplified form,

$$\begin{aligned} G(k_y n l_x l'_x) &= G^{(0)}(k_y n l_x l'_x) + \sum_{l_{x1}, l_{x2} \geq 0} G^{(0)}(k_y n l_x l_{x1}) \\ &\times \Sigma(k_y n l_{x1} l_{x2}) G(k_y n l_{x2} l'_x), \end{aligned} \quad (5.8)$$

where $\Sigma(k_y n l_x l'_x) = \Sigma_{sun}(k_y n l_x l'_x)$. In the diagrammatic form this equation is shown in Fig. 10. In the figure, thin and thick lines indicate the zeroth-order $G^{(0)}$ and full G Green's functions, respectively.

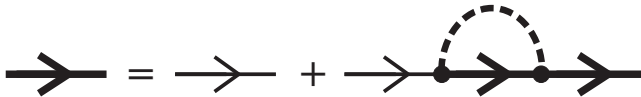


Figure 10: The diagram representation of the Dyson equation (5.8).

Lets us switch from the Matsubara Green's functions to the real-frequency retarded Green's functions. It can be done using the following relations be-

tween these functions:

$$\begin{aligned}
D_{ij}(k_y\nu l_x l'_x) &= \int_{-\infty}^{\infty} \frac{d\omega}{2\pi} \frac{\text{Im}[\hat{D}(k\omega l_x l'_x) + \hat{D}^T(k_y\omega l'_x l_x)]}{\omega - i\omega_\nu} \\
&- i \frac{\text{Re}[\hat{D}(k_y\omega l_x l'_x) - \hat{D}^T(k_y\omega l'_x l_x)]}{\omega - i\omega_\nu}, \\
G(k_y n l_x l'_x) &= \int_{-\infty}^{\infty} \frac{d\omega}{2\pi} \frac{\text{Im}[G(k\omega l_x l'_x) + G(k_y\omega l'_x l_x)]}{\omega - i\omega_n} \\
&- i \frac{\text{Re}[G(k_y\omega l_x l'_x) - G(k_y\omega l'_x l_x)]}{\omega - i\omega_n}
\end{aligned} \tag{5.9}$$

with $D_{ij}^T(k_y\omega l_x l'_x) = D_{ji}(k_y\omega l_x l'_x)$. The relations can be verified using the spectral representation. From the Dyson equation (5.4), self-energy (5.5), and equations below one can see that

$$G(k_y\omega l_x l'_x) = G(k_y\omega l'_x l_x). \tag{5.10}$$

Owing to this equation and Eq. (4.25), the relations between Matsubara and retarded Green's functions (5.9) are simplified,

$$\begin{aligned}
D_{ij}(k_y\nu l_x l'_x) &= \int_{-\infty}^{\infty} \frac{d\omega}{\pi} \frac{\text{Im}D_{ij}(k_y\omega l_x l'_x)}{\omega - i\omega_\nu}, \\
G(k_y n l_x l'_x) &= \int_{-\infty}^{\infty} \frac{d\omega}{\pi} \frac{\text{Im}G(k_y\omega l_x l'_x)}{\omega - i\omega_n}.
\end{aligned} \tag{5.11}$$

By the analytic continuation

$$i\omega_n \rightarrow \omega + i\eta, \quad \eta \rightarrow +0$$

the self-energy equation is transformed to real frequencies,

$$\begin{aligned}
G(k_y\omega l_x l'_x) &= G^{(0)}(k_y\omega l_x l_x) + \sum_{l_{x1}, l_{x2} \geq 0} G^{(0)}(k_y\omega l_x l_{x1}) \\
&\times \Sigma(k_y\omega l_{x1} l_{x2}) G(k_y\omega l_{x2} l'_x).
\end{aligned} \tag{5.12}$$

If we take into account that

$$G^{(0)}(k_y\omega l_x l'_x) = \frac{\delta_{l_x l'_x}}{\omega - \mu'_{l_x}}, \tag{5.13}$$

the Dyson equation (5.12) can be rewritten as

$$G(k_y\omega l_x l'_x) = \frac{1}{\omega - \varepsilon l_x} \left[\delta_{l_x l'_x} + \sum_{l_{x2} \geq 0} \Sigma(k_y\omega l_x l_{x2}) G(k_y\omega l_{x2} l'_x) \right]. \quad (5.14)$$

In order to switch to the real-frequency self-energy one needs to substitute the representations (5.11) into self-energy (5.5) and carry out the summation over ν by using the Poisson summation rule [60],

$$\sum_{\nu=-\infty}^{\infty} F(i\omega\nu) = \frac{\beta}{2\pi i} \int_C \frac{F(\nu)d\nu}{e^{\beta\nu} - 1}. \quad (5.15)$$

Here the contour C encloses the imaginary axis of the frequency plane and within the contour there is no singularities of the function $F(\nu)$. Deforming the contour to infinity, bypassing poles of Green's functions, we find the expression for the imaginary part of the self-energy:

$$\begin{aligned} \text{Im}\Sigma(k_y\omega l_x l'_x) &= -\frac{1}{N_y} \sum_{k'_y} \sum_{s,s'=-1}^1 \theta(l_x + s)\theta(l'_x + s') \\ &\times \int_{-\infty}^{\infty} \frac{d\omega'}{\pi} [n_F(\omega' - \omega) + n_B(\omega')] \\ &\times \text{Im}G(k_y - k'_y, \omega - \omega', l_x + s, l'_x + s') \\ &\times [g_{k_y - k'_y, s} g_{k_y s'} \text{Im}D_{12}(k'_y \omega' l_x, l'_x + s') \\ &+ g_{k_y - k'_y, s} g_{k_y - k'_y, s'} \text{Im}D_{11}(k'_y \omega' l_x, l'_x) \\ &+ g_{k_y s} g_{k_y s'} \text{Im}D_{22}(k'_y \omega', l_x + s, l'_x + s') \\ &+ g_{k_y s} g_{k_y - k'_y, s'} \text{Im}D_{21}(k'_y \omega', l_x + s, l'_x)]. \end{aligned} \quad (5.16)$$

Here $n_F(\omega)$ and $n_B(\omega)$ are the Fermion and Boson occupation numbers, respectively,

$$n_F(\omega) = \frac{1}{e^{\omega/T} + 1}, \quad n_B(\omega) = \frac{1}{e^{\omega/T} - 1}. \quad (5.17)$$

The real part of the self-energy can be calculated from the Kramers-Krönig relation

$$\text{Re}\Sigma(k_y\omega l_x l'_x) = \mathcal{P} \int_{-\infty}^{\infty} \frac{d\omega'}{\pi} \frac{\text{Im}\Sigma(k_y\omega' l_x l'_x)}{\omega' - \omega}, \quad (5.18)$$

where \mathcal{P} stands for the Cauchy principal value.

It is instructive to elucidate how the Dyson equation (5.14) and self-energy

(5.16) are transformed to the form for an unbounded crystal with distance from the boundary. The second-term in the right-hand side of the magnon Green's function (4.12), (4.24) becomes negligibly small *if at least one of the coordinates* l_x or l'_x is larger than two. The Green's function $\hat{D}^{(0)}(k_y\omega l_x l'_x)$ (4.24), to which $\hat{D}(k_y\omega l_x l'_x)$ (4.12) is reduced for such l_x coordinates, contains the multiplier $\sin[k_x(l_x + 1)]\sin[k_x(l'_x + 1)]$ in its integrand [see Eq. (4.24)]. If in this multiplier the sines are replaced by their representation through the exponential functions,

$$\sin(x) = \frac{1}{2i}(e^{ix} - e^{-ix}),$$

one can realise that terms with the same signs of exponents are small for large l_x or l'_x , since the respective exponential functions rapidly oscillate. Remaining terms depend only on the difference $l_x - l'_x$ as must be for the unbounded crystal. It can be shown that these terms are identical to the Green's function for this case. Since the magnon Green's function defines the form of the hole Green's function, one can expect that the latter also becomes close to its unbounded form when at least one of the x coordinates is large. Taking this into account, from the Dyson equation (5.14), self-energy (5.16), Eqs. (4.12) and (4.24) after the Fourier transformations over l_x we obtain the equations for the unbounded crystal (periodic in the Y direction and infinite in the X direction),

$$\begin{aligned} G_b(k_y k_x \omega) &= \frac{1}{\omega - \mu + \Sigma(k_y k_x \omega)}, & (5.19) \\ \text{Im}\Sigma_b(k_y k_x \omega) &= -\frac{16t^2}{N_y} \sum_{k'_y} \frac{1}{2\pi} \int_{-\pi}^{\pi} dk'_x \left\{ \text{Im}G_b(k_x - k'_x, k_y - k'_y, \omega - E_{k'_x k'_y}) \right. \\ &\times \left[n_F(E_{k'_x k'_y} - \omega) + n_B(E_{k'_x k'_y}) \right] \\ &\times \left(\gamma_{k_y - k'_y, k_x - k'_x}^{(2)} u_{k'_x k'_y} + \gamma_{k_y k_x}^{(2)} v_{k'_x k'_y} \right)^2 \\ &- \text{Im}G(k_x - k'_x, k_y - k'_y, \omega + E_{k'_x k'_y}) \\ &\times \left[n_F(-E_{k'_x k'_y} - \omega) + n_B(-E_{k'_x k'_y}) \right] \\ &\times \left. \left(\gamma_{k_x k_y}^{(2)} u_{k'_x k'_y} + \gamma_{k_x - k'_x, k_y - k'_y}^{(2)} v_{k'_x k'_y} \right)^2 \right\}, & (5.20) \end{aligned}$$

where

$$u_{k_y k_x} = \frac{1}{2} \left(\sqrt[4]{\frac{1 - \gamma_{k_y k_x}^{(2)}}{1 + \gamma_{k_y k_x}^{(2)}}} + \sqrt[4]{\frac{1 + \gamma_{k_y k_x}^{(2)}}{1 - \gamma_{k_y k_x}^{(2)}}} \right),$$

$$v_{k_y k_x} = \frac{1}{2} \left(\sqrt[4]{\frac{1 - \gamma_{k_y k_x}^{(2)}}{1 + \gamma_{k_y k_x}^{(2)}}} - \sqrt[4]{\frac{1 + \gamma_{k_y k_x}^{(2)}}{1 - \gamma_{k_y k_x}^{(2)}}} \right).$$

For small hole concentrations, when the second term in braces in Eq. (5.20) can be neglected, equations (5.19) and (5.20) become identical to the equations obtained for an unbounded lattice (2.19), (2.20) [45, 50].

For the numerical calculations it is convenient to restrict the coordinates l_x and l'_x within the range $[0, l_{xm}]$ in the Dyson equation (5.14) and to rewrite this equation in a more tractable form

$$\sum_{l''_x=0}^{l_{xm}} [(\omega - \varepsilon_{l_x})\delta_{l_x l''_x} - \Sigma(k_y \omega l_x l''_x)] G(k_y \omega l''_x l'_x) = \delta_{l_x l'_x} + M(k_y \omega l_x l'_x), \quad (5.21)$$

where

$$M(k_y \omega l_x l'_x) = \sum_{l''_x > l_{xm}} \Sigma(k_y \omega l_x l''_x) G(k_y \omega l''_x l'_x). \quad (5.22)$$

The parameter l_{xm} is expected to be large enough for substituting the self-energy and Green's function in Eq. (5.22) by their values in an unbounded crystal, $\Sigma_b(k_y \omega l_x l'_x)$ and $G_b(k_y \omega l_x l'_x)$, in compliance with the above discussion. At the same time l_{xm} can be chosen to be small enough for the inversion of the matrix in the left-hand side of Eq. (5.21) to not lead to time-consuming calculations.

5.2 The hole spectrum

In the below calculations we set $T = 0$ and $J/t = 0.2$. The latter ratio of parameters was selected from the range $[0.1 - 0.4]$ derived for hole-doped cuprates from the many-band Hubbard model of the Cu-O plane [61, 62]. Equations (5.21) and (5.22) were solved by iterations for $l_{xm} = 4$, using as the starting function for $G(k_y \omega l_x l'_x)$ Green's function for an unbounded crystal $G_b(k_y \omega l_x l'_x)$. To ensure the convergence of the iteration procedure an artificial broadening was introduced by substituting ω with $\omega + i\eta$, $\eta = 0.05t$, in Eq. (5.21). The chemical potential μ was chosen so that the frequency $\omega = 0$, which separates occupied and unoccupied states, was located in the low-frequency tail of the spectral function

$$A(k_y \omega l_x) = -\text{Im}G(k_y \omega l_x l_x). \quad (5.23)$$

This ensures a low hole concentration expected in the derivation of the above formulas.

The spectral function gives the density of states projected on states of the row l_x . A typical example of this quantity obtained in the course of the calcu-

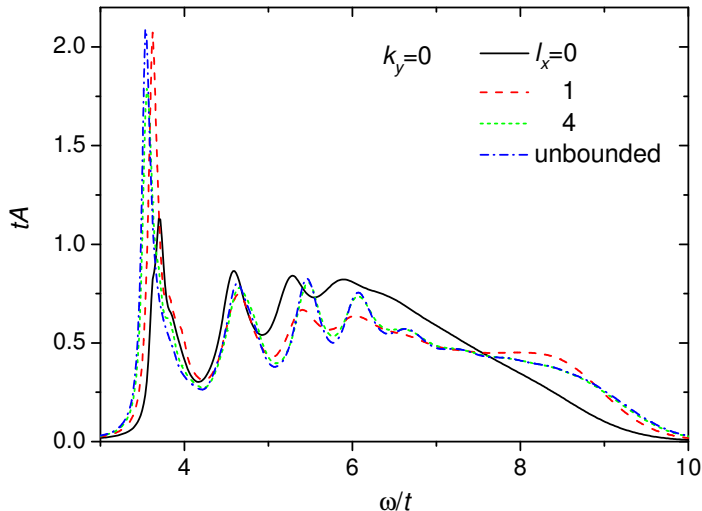


Figure 11: The spectral function $A(k_y\omega l_x)$ for $k_y = 0$, $l_x = 0, 1, 4$ and in an unbounded crystal $A_b(k_y\omega 0)$.

lations is shown in Fig. 11¹. Besides the spectral function for near-boundary rows, Fig. 11 contains also the spectral function of the unbounded crystal,

$$A_b(k_y\omega, l_x - l'_x) = -\frac{1}{2\pi} \int_{-\pi}^{\pi} dk_x \cos[k_x(l_x - l'_x)] \text{Im}G_b(k_y k_x \omega), \quad (5.24)$$

which is given for comparison. Due to the translation symmetry this function depends only on the difference $l_x - l'_x$ and for the considered case $l_x = l'_x$ its last argument is zero. In shape this function resembles spectral functions obtained for a fixed wavevector (k_x, k_y) in an unbounded crystal [45, 50]. However, the maxima in Fig. 11 are somewhat broadened in comparison with these functions due to the integration over k_x in Eq. (5.24). As would be expected, the spectrum in the boundary row $l_x = 0$ differs most greatly from $A_b(k_y\omega 0)$. From the figure one can see how the spectrum is transformed, gradually approaching to the spectrum of an unbounded crystal, with the distance from the boundary. In the scale of Fig. 11 already the spectrum in the fifth row ($l_x = 4$) is barely distinguishable from $A_b(k_y k_x 0)$.

The vicinity of the main maximum of the spectral function is shown in Fig. 12 for several wavevectors. From the above formulas it can be shown that $A(k_y\omega l_x) = A(\pi - k_y, \omega l_x)$. Besides, in accord with the symmetry $A(k_y\omega l_x) = A(-k_y, \omega l_x)$. Therefore, we selected wavevectors k_y from the range $[0, \pi/2]$. From these figures and equations one can see that the spectral maxima are

¹It is worth noting that the shape of the spectral function is markedly changed only when the frequency of the main maximum ω_m becomes close to $\omega = 0$ [63]. Thus, nearly the same spectral function as shown in Fig. 11 is obtained for any chemical potential for which $\omega_m \gtrsim t$.

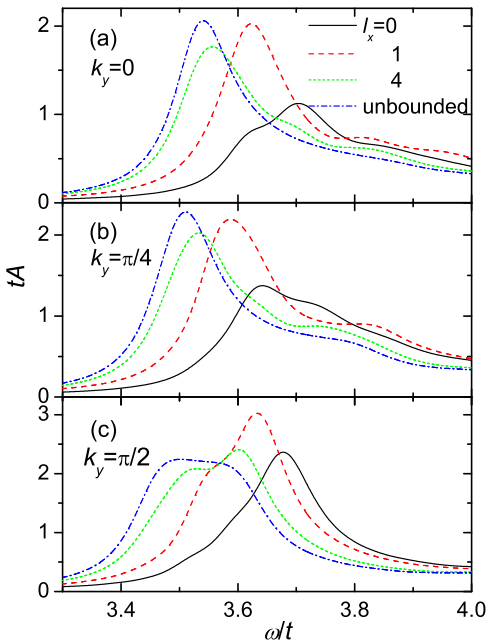


Figure 12: The spectral function $A(k_y\omega l_x)$ in the vicinity of the main maximum for $k_y = 0$ (a), $\pi/4$ (b) and $\pi/2$ (c) in the rows $l_x = 0, 1, 4$ and in an unbounded crystal $A_b(k_y\omega 0)$.

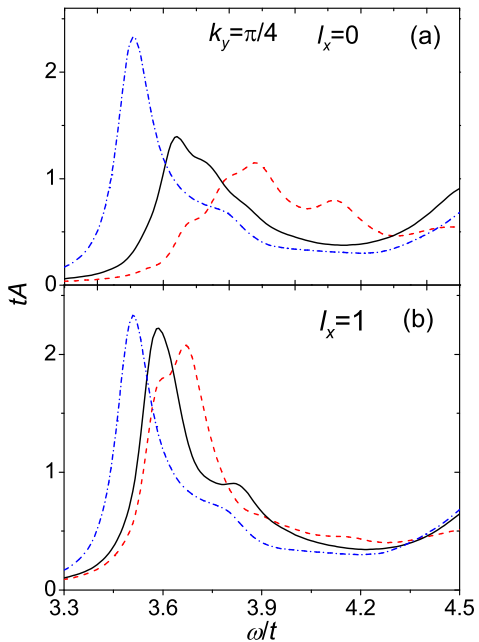


Figure 13: The spectral function $A(k_y\omega l_x)$ in the vicinity of the main maximum with taking into account the boundary magnon mode (black solid lines) and without it (red dashed lines) for $k_y = \pi/4$, $l_x = 0$ (a) and 1 (b). Blue dash-dotted lines corresponds to $A_b(k_y\omega 0)$.

shifted to higher frequencies on approaching the boundary for all wavevectors k_y . In accordance with this the low-frequency tails of the maxima become weaker with decreasing l_x . Since the concentration of holes in a row l_x is determined by this tail,

$$x(l_x) = \frac{1}{N_y} \sum_{k_y} \langle h_{k_y l_x}^\dagger h_{k_y l_x} \rangle = \frac{1}{N_y} \sum_{k_y} \int_{-\infty}^{\infty} \frac{d\omega}{\pi} A(k_y\omega l_x) n_F(\omega),$$

one concludes that the concentration decreases monotonically on approaching the boundary – *near-boundary rows are depleted of holes*.

To elucidate a formation mechanism of this hole depletion layer it is worth noting that the near-boundary region has three differences from the bulk crystal: (i) the attraction of an immobile hole to the boundary, (ii) the domination of the near-boundary magnon mode in the spectrum, and (iii) the shape of a spin polaron. These peculiarities can be expected to influence the population

of holes in the near-boundary region.

As for the first possible factor, the calculations show that the omission of the attraction term is barely perceptible in the shape and location of maxima of the spectral function. This conclusion can be also drawn from Figs. 11 and 12 and from the fact that for the chosen chemical potential, the energy of an immobile hole is equal to $6t$. As seen in these figures, by virtue of the hole-magnon interactions there is an energy gain equal approximately to $2.5t$ in the states corresponding to the main maximum. Since the attraction is of the order of $J \ll t$, much smaller than the energy gain, it cannot play any role in the hole distribution.

The contribution of the second factor, the near-boundary magnon mode, can be estimated from Fig. 13. The spectral function without this mode was calculated with the magnon Green's function (4.12) instead of the full function (4.24). As seen from the figure, the inclusion of the near-boundary mode decreases the frequency of the main maximum and redistributes the spectral intensity. The largest frequency shift is observed for the boundary row. Thus, the contribution of the near-boundary mode is essential for the formation of charge carriers near the boundary. However, the sign of the frequency shift given by this mechanism is opposite to the one observed in Figs. 11 and 12. Therefore, the third of the mentioned factors, the shape of the magnon cloud of the spin polaron, is of primary importance in the formation of the depletion layer.

As known, in the considered model holes form spin polarons [45, 50]. Due to the antiferromagnetic background a hole can move over the lattice only with the emission and absorption of magnons, as seen from Hamiltonian (3.19). As a consequence the hole is surrounded by a cloud of magnons. Without the antiferromagnetically ordered spins the maximum energy gain, which a moving hole can achieve in comparison with an immobile quasiparticle, is $4t$ – the difference between the lowest energy in the 2D nearest-neighbor band and its center of mass. In the antiferromagnetic lattice this gain is decreased by the energy consumption for the distortion of the magnetic order around the hole. For the ratio $J/t = 0.2$ the energy gain is reduced approximately to $2.5t$ (see Figs. 11 and 12). This energy gain is still comparable with the maximal possible value $4t$. This large energy gain complicates the formation of ferrons - ferromagnetically ordered regions around holes - and stripes or a phase separation in the t - J model. Only for ratios J/t which are much smaller than those corresponding to hole-doped cuprates, the gain in the hole kinetic energy in the ferromagnetic region is large enough to stabilize ferrons [52, 53, 64, 65]. On the other hand, a phase separation is observed for practically immobile holes at much larger $J/t > 1$ [34].

Away from the boundary the magnon cloud of the spin polaron has the symmetry determined by the group of the hole wavevector and this symmetry ensures the lowest energy of the spin polaron. Near the boundary, the bulk crystal symmetry is violated and the cloud is distorted, which inevitably leads

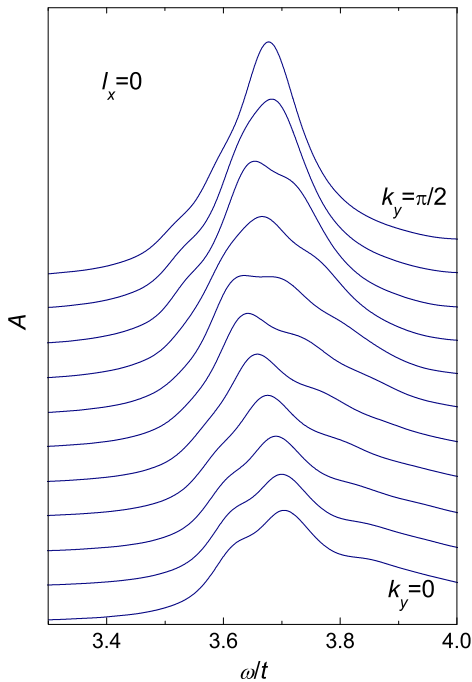


Figure 14: The spectral function $A(k_y\omega l_x)$ in the vicinity of the main maximum for $l_x = 0$ and k_y ranging from 0 (the bottom curve) to $\pi/2$ (the upper curve) with the step $\pi/20$. For better visibility curves with larger k_y are shifted upward with respect to curves with smaller wave vectors.

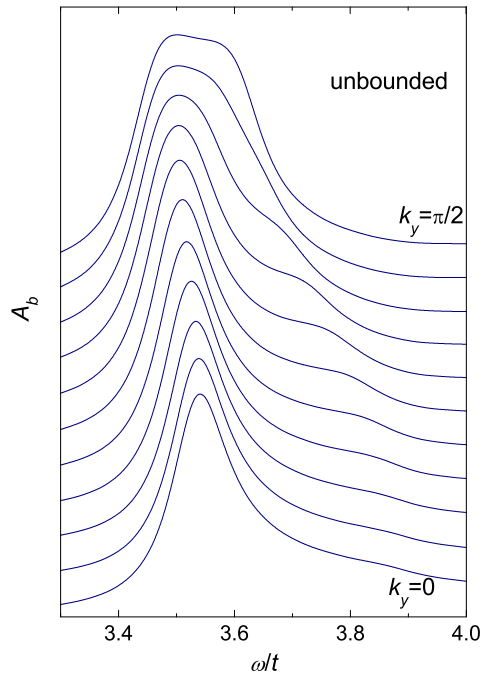


Figure 15: The same as Fig. 14, but for the spectral function of an unbounded crystal $A_b(k_y\omega 0)$.

to a growth of the energy. Thus, it is energetically unfavorable for a hole to reside near the boundary. This is just the mechanism of the formation of the depletion layer in the considered model. The extent of the cloud deformation near the boundary can be estimated from the shift of the main spectral maximum in a given row with respect to its bulk counterpart. For the boundary row and $J/t = 0.2$ this shift is of the order of J (see Fig. 12) and is comparable with the spin-polaron bandwidth $2J$. This fact points to a strong distortion of the magnon cloud near the boundary. The depth of the row in which the location of the main maximum practically coincides with that in an unbounded crystal gives an estimate of the size of the magnon cloud. In our case, its radius is approximately equal to four lattice spacings.

Closer inspection of the obtained spectral functions shows that the main maximum for the boundary row has a more complicated structure than spectra for $l_x = 2-4$ and for an unbounded crystal. Figures 14 and 15 demonstrate this

difference. The evolution of maxima in rows $l_x = 2-4$ is similar to that shown in Fig. 15, while for $l_x = 1$ the spectrum has some additional peculiarities like in the case $l_x = 0$. The behaviour of the spectral features in the latter figure can be understood from the known dispersion of the spin polaron in an unbounded crystal [45, 50]. This dispersion has a minima at wavevectors $(\pm\frac{\pi}{2}, \pm\frac{\pi}{2})$ and it is weak on the boundary of the magnetic Brillouin zone, which is composed of segments $(0, \pm\pi)-(\pm\pi, 0)$. The states near these segments make the main contribution to the maximum in Fig. 15 – for $k_y = 0$ wavevectors of these states lie near $(\pm\pi, 0)$, while for $k_y = \frac{\pi}{2}$ these wave vectors are from the neighborhood of $(\pm\frac{\pi}{2}, \frac{\pi}{2})$. The change in the location of the maximum when k_y grows from 0 to $\frac{\pi}{2}$ in Fig. 15 reflects the mentioned weak dispersion of the states along the boundary of the magnetic Brillouin zone. The shoulder, which approaches the maximum from high frequencies, is mainly connected with states from the vicinity of the axes and the boundary of the Brillouin zone – for $k_y = \frac{\pi}{2}$ these states have wavevectors near $(0, \frac{\pi}{2})$ and $(\pm\pi, \frac{\pi}{2})$. At least two high-frequency shoulders can be revealed in Fig. 14. Additionally the main maximum in the boundary row has also a low-frequency shoulder which is best seen for small k_y . As follows from Fig. 12(a), the location of this latter shoulder is close to the position of the maximum in the row $l_x = 1$. Indeed, in the considered system two neighboring rows have maxima, which are shifted in the frequency scale relative to each other. Since in accord with the Dyson equation (5.8) the spectral function of a given row is connected with the functions in neighboring rows, one can expect that a replica of the more intensive maximum for $l_x = 1$ will be seen in the boundary row. In the present case this replica looks like the low-frequency shoulder of the main maximum. Conceivably the presence of the additional high-frequency shoulders is also connected with the deeper row. Thus, a more complicated character of the boundary spectra is connected with the replica of the maximum of the underlying row. Notice that this replica is an attendant effect of the hole depletion in the near-boundary region.

From the similarity of the 2D and 3D magnon spectra [54, 59, 66] we can expect to obtain analogous results for charge carriers in a 3D crystal with strong electron correlations. From these results, the conclusion can be drawn that even in the considered case of the idealized surface the spectral function at the boundary may essentially differ from the bulk spectrum. This function can have additional features and shifts which, among other things, are connected with a deformation of polarons near the surface. Notice, however, that the influence of the boundary on the magnon spectra [66] and presumably on the hole spectral functions is more pronounced in the considered 2D case than in the 3D case. The discrepancies between the photoemission data of a number of transition-metal oxides and calculated bulk spectra [67, 68] may be connected with the discussed effects.

Comparing results obtained in the semi-infinite Hubbard model [22–26] with our results, we find some similar features. In spite of the differences of models and computation methods, in both models for uniform parameters

the quasiparticle weight is lowered, while the intensity of the high-energy part of the spectrum grows [23] at the boundary. The reason for this intensity redistribution is similar – it is a reduced coordination number at the boundary, which leads to an effective strengthening of the on-site repulsion in the Hubbard model and to the deformation of the magnon cloud around the hole in the spin polaron in the t - J model.

Summary

In the last few years, an active interest is taken in the behavior of elementary excitations near a junction of a strongly correlated crystal with another crystal or vacuum. Crystals with strong electron correlations are usually characterized by magnetic ordering, which plays a large role in the properties of charge carriers. Our study was aimed at the investigation of the influence of a crystal boundary on elementary excitations in such a crystal.

Firstly, the influence of the boundary on magnetic excitations and nearest-neighbor spin correlations of a semi-infinite two- and three-dimensional spin- $\frac{1}{2}$ Heisenberg antiferromagnets was considered. Notice that the Hubbard model, widely used for the description of strongly correlated systems, is reduced to the Heisenberg model at half-filling and in the limit of large Hubbard repulsions. Two-dimensional square and three-dimensional simple cubic lattices were considered with the boundary oriented perpendicular to one of the crystal axes. The spin-wave approximation was applied for zero temperature.

The main results are the following:

- The presence of the boundary divides the antiferromagnet into near-boundary and bulk regions which are characterized by different dominant spin excitations. The spectrum of the near-boundary region, which is formed by the first two rows/layers of spins nearest to the boundary, consists of a $(d-1)$ -dimensional mode of near-boundary spin waves. Here $d = 2$ or 3 is the dimensionality of the antiferromagnet. Excitations of the rest of the antiferromagnet are d -dimensional standing spin waves.
- The description of perturbations introduced by the boundary into the spectrum of spin excitations is in many respects similar to the problem of a local defect in a crystal. In this latter problem, the perturbation also divides the crystal into two regions with different elementary excitations - a vicinity of the defect with localized states and the rest of the crystal with bulk states.
- Near-boundary mode of spin waves leads to the appearance of comb-like pattern of nearest-neighbor spin correlations in the near-boundary region: the correlations on the boundary and between the boundary and the second to the boundary layers are in absolute value larger than in the bulk, while in the second layer and between the second and the third layers the correlations are smaller than in the bulk. Enhancement of spin correlations on the boundary is caused by the lower dimensionality of the near-boundary mode in comparison with the bulk mode.
- In regard to the influence of the dimensionality of an antiferromagnet on spin correlations, qualitative dependencies of spin correlations on the distance from the boundary are similar for the 2D and 3D cases. However, there is a quantitative difference. In the 2D case the deviations from the

bulk value are greater than in the 3D case – in the former case the largest deviation is equal to 12% in comparison with 5% in the latter.

Secondly, the influence of the boundary on charge carriers in a semi-infinite two-dimensional t - J model was considered. For this purpose, the hole spectral function was calculated using the spin-wave and non-crossing approximations for the case of small hole concentrations and zero temperatures.

The main results are the following:

- The near-boundary region – several near-boundary site rows– is depleted of holes. The formation of this depletion layer is caused by a deformation of the magnon cloud, which surrounds the hole, near the boundary. The deformation of a cloud leads to a growth of the energy of the spin polaron.
- The hole depletion leads to a more complicated spectral function in the near-boundary row in comparison with its bulk shape - the main maximum may have additional low-frequency and high-frequency shoulders. This is a consequence of a difference in the spectral functions for near-boundary rows - replicas of maxima from these rows are seen in the boundary spectral function.

Summary in Estonian

Elementaarergastused tugevalt korreleeritud kristalli pinna lähedal

Viimastel aastatel on ilmnenud aktiivne huvi elementaarergastuste käitumise iseärasuste vastu tugevalt korreleeritud kristalli äärelähedases piirkonnas ning kahest kristallist koosneva heterostruktuuri eralduspinnalähedases piirkonnas juhul, kui vähemalt üks kristallidest on tugevate elektronkorrelatsioonidega. Tugevate elektronkorrelatsioonidega kristallidele on tavaliselt iseloomulik magnetiline korrastatus, mis mängib suurt rolli laengukandjate käitumises. Doktoriväitekirja eesmärgiks oli uurida kristalli ääre(pinna) mõju elementaarergastustele sellises kristallis.

Esiteks, on uuritud äärepinna mõju magnetilistele ergastustele ja lähinaabrite spinnide korrelatsioonidele poollõpmatutes kahe- ja kolmemõõtmelistes Heisenbergi spinn- $\frac{1}{2}$ antiferromagneetikutes. Tasub märkida, et Hubbard mudel, mida laialt kasutatakse tugevalt korreleeritud süsteemide kirjeldamiseks, on taandatav Heisenbergi mudelile pooltäidetud juhul ning tugeva Hubbard'i tõukumise piirjuhul. Ruutvõret ja lihtsat kuubilist võret käsitleti juhul, kui äär oli risti ühega kristalli telgedest. Spinnlaine lähendust kasutati nulltemperatuuril.

Põhilised tulemised on järgmised:

- Ääre(pinna) olemasolu jagab antiferromagneetiku äärelähedaseks piirkonnaks ja kristalli sügavuseks, mis on iseloomustatud erinevate dominantsete spinn-ergastustega. Äärelähedases piirkonnas, mille moodustavad spinnide kaks äärele lähimat rida/kihti, koosneb spekter spinni ääre-pindlainete ($d - 1$)-mõõtmelisest moodist. Siin $d = 2$ või 3 on antiferromagneetiku dimensioonid. Antiferromagneetiku ülejäänud osa ergastused on d -mõõtmelised seisvad spinnlained.
- Ääre poolt indutseeritud häirituste kirjeldamine spinn-ergastuste spektris on paljudes aspektides sarnane lokaalse defekti probleemiga. Viimasel juhul on kristall häirituse poolt samuti jagatud kahte ossa, kus elementaarergastused on erinevad - defektilähedane osa lokaliseeritud olekutega ja kristalli ülejäänud osa ruumiliste olekutega.
- Spinni ääre-pindlainete mood põhjustab spinnide korrelatsioonide kammstruktuuri moodustumist äärelähedases piirkonnas: korrelatsioonid äärel ning ääre ja teise kihi vahel on absoluutväärtuselt suuremad kui kristalli sügavuses, seevastu teises ning teise ja kolmanda kihi vahel on korrelatsioonid absoluutväärtuselt väiksemad kui kristalli sügavuses. Spinnide korrelatsioonide tugevnemine äärel on põhjustatud spinni ääre-pindlaine moodi madalamast dimensioonist.

- Mis puutub antiferromagneetiku dimensiooni mõjusse spinnide korrelatsioonidele, spinnide korrelatsioonide kvalitatiivsed sõltuvused kaugusest äärest on sarnased, kuid on olemas üks kvantitatiivne erinevus. Nimelt, kahemõõtmelisel juhul on kõrvalekalded väärtusest kristalli sügavuses suuremad kui kolmemõõtmelisel juhul – kahemõõtmelisel juhul suurim kõrvalekalle on 12% ja kolmemõõtmelisel juhul - 5%.

Teiseks, on uuritud ääre mõju laengukandjatele poollõpmatus kahemõõtmelises t - J mudelis. Selle eesmärgiga arvutati augu spektraalfunktsioon, kasutades spinnlaine lähendust ja Born'i lähendust aukude madalate kontsentratsioonide korral nulltemperatuuril.

Põhilised tulemused on järgmised:

- Äärelähedane piirkond – mõned äärelähedased read – on aukudest vaesed. Suikekihi moodustumine on põhjustatud augu ümbritseva magnonpilve deformatsioonist äärelähedases piirkonnas. Pilve deformatsioon viib spinnpolaroni energia kasvuni.
- Aukudest vaesustus põhjustab ääre spektraalfunktsiooni keerulisemat kuju võrreldes kristalli sügavusega - peamaksimumil võivad olla madal- ja kõrgsageduslikud lisaõlad. Ääre spektraalfunktsiooni keerulisem kuju on tingitud äärelähedaste ridade spektraalfunktsioonide erinevusest - nende ridade maksimumide kosterd on nähtavad ääre spektraalfunktsioonis.

Acknowledgements

First of all, I am sincerely grateful to my supervisor, Alexei Sherman, for introducing me to the fascinating field of physics of strong electron correlations and initiating these studies. His wide and deep knowledge, and experience have been extremely important for the progress of research. During our collaboration he has been a pleasant teacher, willing to share knowledge, experience and passion for physics of strongly correlated electron systems. His enthusiasm and passion has been a source of inspiration for my studies. Timely feedback, continuous help and advice are highly appreciated. Thank you very much for continuous support, warm encouragement, kindness, and believing in me. I am really fortunate to have had such a fabulous supervisor to go through this journey.

I thank all the colleagues of the Laboratory of Solid State Theory at the Institute of Physics for creating pleasant and friendly atmosphere.

I am indebted to my previous supervisors, Teet Örd and Risto Tammelo, for introducing me to the topic of stochastic processes and collaboration. I appreciate the opportunity to gain a wider breadth of experience.

Sincere gratitude goes to all my teachers who have educated me during my university studies.

This work has been partially supported by the Estonian Ministry of Education and Research (Target Financed Project No 0180013s07), the Estonian Science Foundation (Grant No 6918), the Tartu University Foundation (Kaleva Travel scholarship), and graduate school "Functional Materials and Processes" receiving funding from the European Social Fund under project 1.2.0401.09-0079 in Estonia.

Appendix: The relation between the spin correlation and Green's function

In order to obtain the relation between the correlation function $\langle \hat{B}_{\mathbf{k}l_x} \hat{B}_{\mathbf{k}l'_x}^\dagger \rangle$ and the matrix magnon Green's function $\hat{D}(\mathbf{k}\omega l_x l'_x)$ (4.12) let us use their definitions

$$\langle \hat{B}_{\mathbf{k}l_x} B_{\mathbf{k}l'_x}^\dagger \rangle = Z^{-1} \sum_{i,j} e^{-E_i\beta} \langle i | \hat{B}_{\mathbf{k}l_x} | j \rangle \langle j | \hat{B}_{\mathbf{k}l'_x}^\dagger | i \rangle, \quad (\text{A.1})$$

$$\hat{D}(\mathbf{k}\omega l_x l'_x) = -i\theta(t)Z^{-1} \sum_i e^{-E_i\beta} \langle i | \left[B_{\mathbf{k}l_x}(t), B_{\mathbf{k}l'_x}^\dagger \right] | i \rangle, \quad (\text{A.2})$$

where E_i , $|i\rangle$ and $|j\rangle$ are eigenenergies and eigenfunctions of the Hamiltonian.

Taking into account that $e^{iHt}|i\rangle = e^{iE_it}|i\rangle$, Green's function (A.2) can be rewritten as

$$\begin{aligned} \hat{D}(\mathbf{k}t l_x l'_x) &= -i\theta(t)Z^{-1} \sum_{ij} \left(e^{-E_i\beta} - e^{-E_j\beta} \right) e^{i(E_i - E_j)t} \\ &\quad \times \langle i | \hat{B}_{\mathbf{k}l_x} | j \rangle \langle j | \hat{B}_{\mathbf{k}l'_x}^\dagger | i \rangle \end{aligned} \quad (\text{A.3})$$

Performing here the Fourier transformation we obtain

$$\hat{D}(\mathbf{k}\omega l_x l'_x) = Z^{-1} \sum_{ij} \left(e^{-E_i\beta} - e^{-E_j\beta} \right) \frac{\langle i | \hat{B}_{\mathbf{k}l_x} | j \rangle \langle j | \hat{B}_{\mathbf{k}l'_x}^\dagger | i \rangle}{\omega + E_i - E_j + i\eta}, \quad (\text{A.4})$$

where we used the following relation

$$\int_{-\infty}^{\infty} dt \theta(t) e^{i(\omega + E_i - E_j)t} = -\frac{1}{i(\omega + E_i - E_j + i\eta)}.$$

Exploiting definition of a Hermitian conjugate operator, $\langle i | \hat{A} | j \rangle^* = \langle j | \hat{A}^\dagger | i \rangle$, we can write

$$Z^{-1} \sum_{ij} \left(e^{-E_i\beta} - e^{-E_j\beta} \right) \frac{\left(\langle i | \hat{B}_{\mathbf{k}l_x} | j \rangle \langle j | \hat{B}_{\mathbf{k}l'_x}^\dagger | i \rangle \right)^*}{\omega + E_i - E_j + i\eta} = \hat{D}^T(\mathbf{k}\omega l'_x l_x), \quad (\text{A.5})$$

where $D_{ij}^T(\mathbf{k}\omega l_x l'_x) = D_{ji}(\mathbf{k}\omega l_x l'_x)$.

Considering that

$$\frac{1}{x \pm i\eta} = \mathcal{P} \frac{1}{x} \mp i\pi\delta(x),$$

we get

$$\begin{aligned}
\text{Im} \left[\hat{D}(\mathbf{k}\omega l_x l'_x) + \hat{D}^T(\mathbf{k}\omega l'_x l_x) \right] &= -2\pi Z^{-1} \sum_{i,j} e^{-E_i\beta} \left(1 - e^{-\omega\beta} \right) \\
&\quad \times \delta(\omega + E_i - E_j) \text{Re} \left[\langle i | \hat{B}_{\mathbf{k}l_x} | j \rangle \langle j | \hat{B}_{\mathbf{k}l'_x}^\dagger | i \rangle \right], \\
\text{Re} \left[\hat{D}(\mathbf{k}\omega l_x l'_x) - \hat{D}^T(\mathbf{k}\omega l'_x l_x) \right] &= 2\pi Z^{-1} \sum_{i,j} e^{-E_i\beta} \left(1 - e^{-\omega\beta} \right) \\
&\quad \times \delta(\omega + E_i - E_j) \\
&\quad \times \text{Im} \left[\langle i | \hat{B}_{\mathbf{k}l_x} | j \rangle \langle j | \hat{B}_{\mathbf{k}l'_x} | i \rangle \right]. \tag{A.6}
\end{aligned}$$

Using the property of the Dirac's delta function,

$$\int_{-\infty}^{\infty} dx f(x) \delta(x - x_0) = f(x_0),$$

we obtain the following expressions for the real and imaginary parts of the correlation function:

$$\begin{aligned}
\text{Re} \langle \hat{B}_{\mathbf{k}l_x} \hat{B}_{\mathbf{k}l'_x}^\dagger \rangle &= \int_{-\infty}^{\infty} \frac{d\omega}{2\pi} \frac{\text{Im} \left[\hat{D}(\mathbf{k}\omega l_x l'_x) + \hat{D}^T(\mathbf{k}\omega l'_x l_x) \right]}{e^{-\omega\beta} - 1}, \\
\text{Im} \langle \hat{B}_{\mathbf{k}l_x} \hat{B}_{\mathbf{k}l'_x}^\dagger \rangle &= \int_{-\infty}^{\infty} \frac{d\omega}{2\pi} \frac{\text{Re} \left[\hat{D}(\mathbf{k}\omega l_x l'_x) - \hat{D}^T(\mathbf{k}\omega l'_x l_x) \right]}{1 - e^{-\omega\beta}}. \tag{A.7}
\end{aligned}$$

Due to the property of Green's function (4.25) we obtain the simpler relation (4.29) connecting Green's function and the correlation function,

$$\langle \hat{B}_{\mathbf{k}l_x} \hat{B}_{\mathbf{k}l'_x}^\dagger \rangle = \int_{-\infty}^{\infty} \frac{d\omega}{\pi} \frac{\text{Im}[\hat{D}(\mathbf{k}\omega l_x l'_x)]}{e^{-\omega\beta} - 1}. \tag{A.8}$$

References

- [1] M. Prutton, *Introduction to Surface Physics* (Clarendon Press, Oxford, 1994).
- [2] W. Shockley, Phys. Rev. **56**, 317 (1939).
- [3] K. Oura, V. G. Lifshits, A. A. Saranin, A. V. Zotov, and M. Katayama, *Surface Science* (Springer-Verlag, Berlin Heidelberg New York, 2003).
- [4] I. E. Tamm, Phys. Z. Soviet Union **1**, 733 (1932).
- [5] S. G. Davison and J. D. Levine, Solid State Phys. **25**, 1 (1970).
- [6] T. Y. Saks and G. S. Zavt, Solid State Phys. **19**, 1856 (1977).
- [7] T. Saks, Proceedings of the Estonian Academy of Sciences. Physics. Mathematics **32**, 388 (1983).
- [8] I. Lifshits, Sov. Phys. Usp. **7**, 549 (1965).
- [9] A. A. Maradudin, Solid State Phys. **18**, 273 (1966).
- [10] A. A. Maradudin, Solid State Phys. **19**, 1 (1967).
- [11] E. Dagotto, Science **318**, 1076 (2007).
- [12] A. Ohtomo, D. A. Muller, J. L. Grazul, and H. Y. Hwang, Nature **419**, 378 (2002).
- [13] A. Ohtomo and H. Y. Hwang, Nature **427**, 423 (2004).
- [14] S. Okamoto and A. J. Millis, Nature **428**, 630 (2004).
- [15] S. S. Kancharla and E. Dagotto, Phys. Rev. B **74**, 195427 (2006).
- [16] W.-C. Lee and A. H. MacDonald, Phys. Rev. B **74**, 075106 (2006).
- [17] N. Reyren, S. Thiel, A. D. Caviglia, L. Fitting Kourkoutis, G. Hammerl, C. Richter, C. W. Schneider, T. Kopp, A. S. Rüetschi, D. Jaccard, M. Gabay, D. A. Muller, J. M. Triscone, and J. Mannhart, Science **317**, 1196 (2007).
- [18] S. Gariglio, N. Reyren, A. D. Caviglia, and J. M. Triscone, Journal of Physics Condensed Matter **21** (2009).
- [19] H. Nakamura, H. Takagi, I. H. Inoue, Y. Takahashi, T. Hasegawa, and Y. Tokura, Appl. Phys. Lett. **89** (2006).
- [20] I. Bloch, J. Dalibard, and W. Zwerger, Rev. Mod. Phys. **80**, 885 (2008).

- [21] M. Snoek, I. Titvinidze, C. Toke, K. Byczuk, and W. Hofstetter, *New J. Phys.* **10** (2008).
- [22] H. Hasegawa, *J. Phys.: Condens. Matter* **4**, 1047 (1992).
- [23] M. Potthoff and W. Nolting, *Z. Phys. B* **104**, 265 (1997).
- [24] M. Potthoff and W. Nolting, *Phys. Rev. B* **59**, 2549 (1999).
- [25] M. Potthoff and W. Nolting, *Phys. Rev. B* **60**, 7834 (1999).
- [26] H. Ishida and A. Liebsch, *Phys. Rev. B* **79**, 045130 (2009).
- [27] J. E. Hirsch, *Phys. Rev. B* **31**, 4403 (1985).
- [28] Y. A. Izyumov, *Phys.-Usp.* **40**, 445 (1997).
- [29] A. V. Mahajan, H. Alloul, G. Collin, and J. F. Marucco, *Phys. Rev. Lett.* **72**, 3100 (1994).
- [30] M. Takigawa, N. Motoyama, H. Eisaki, and S. Uchida, *Phys. Rev. B* **55**, 14129 (1997).
- [31] K. H. Höglund and A. W. Sandvik, *Phys. Rev. B* **79**, 020405(R) (2009).
- [32] M. A. Metlitski and S. Sachdev, *Phys. Rev. B* **78**, 174410 (2008).
- [33] T. Pardini and R. R. P. Singh, *Phys. Rev. B* **79**, 094413 (2009).
- [34] E. Dagotto, *Rev. Mod. Phys.* **66**, 763 (1994).
- [35] D. Zubarev, *Sov. Phys. Usp.* **3**, 320 (1960).
- [36] A. A. Abrikosov, L. P. Gorkov, and I. E. Dzyaloshinsky, *Methods of Quantum Field Theory in Magnetism* (Pergamon Press, Oxford, 1965).
- [37] G. D. Mahan, *Many-particle Physics* (Plenum Press, New York, 1990).
- [38] T. Matsubara, *Prog. Theor. Phys.* **14**, 351 (1955).
- [39] G. C. Wick, *Phys. Rev.* **80**, 268 (1950).
- [40] J. Hubbard, *Proc. R. Soc. Lond. A* **276**, 238 (1963).
- [41] J. Hubbard, *Proc. R. Soc. Lond. A* **277**, 237 (1964).
- [42] P. W. Anderson, *Science* **235**, 1196 (1987).
- [43] K. A. Chao, J. Spalek, and A. M. Oles, *J. Phys. C* **10** (1977).
- [44] K. A. Chao, J. Spalek, and A. M. Oles, *Phys. Rev. B* **18**, 3453 (1978).

- [45] F. Marsiglio, A. E. Ruckenstein, S. Schmitt-Rink, and C. M. Varma, *Phys. Rev. B* **43**, 10882 (1991).
- [46] J. Appel, *Solid State Phys.* **21**, 193 (1968).
- [47] Y. A. Izyumov and Y. N. Skryabin, *Statistical Mechanics of Magnetically Ordered Systems* (Consultants Bureau, New York, 1988).
- [48] S. Ovchinnikov and V. Valkov, *Hubbard Operators in the Theory of Strongly Correlated Electrons* (Imperial College Press, London, 2004).
- [49] J. E. Hirsch, *Phys. Rev. Lett.* **59**, 228 (1987).
- [50] G. Martinez and P. Horsch, *Phys. Rev. B* **44**, 317 (1991).
- [51] S. Tyablikov, *Methods of the Quantum Theory of Magnetism* (Plenum Press, New York, 1967).
- [52] A. V. Sherman, *Physica C* **171**, 395 (1990).
- [53] J. Sabczynski, M. Schreiber, and A. Sherman, *Phys. Rev. B* **48**, 543 (1993).
- [54] A. Sherman and N. Voropajeva, *Int. J. Modern Phys. B* **24**, 979 (2010).
- [55] G. Korn and T. Korn, *Mathematical Handbook for Scientists and Engineers* (McGraw-Hill Book Company, New York, 1961).
- [56] C. J. Hamer, W. Zheng, and P. Arndt, *Phys. Rev. B* **46**, 6276 (1992).
- [57] I. G. Gochev, *Phys. Rev. B* **47**, 1096 (1993).
- [58] J. Oitmaa, C. J. Hamer, and W. Zheng, *Phys. Rev. B* **50**, 3877 (1994).
- [59] N. Voropajeva and A. Sherman, *Phys. Lett. A* **373**, 3473 (2009).
- [60] Schrieffer, *Theory of Superconductivity* (Perseus Books, Reading, MA, 1991).
- [61] A. K. McMahan, J. F. Annett, and R. M. Martin, *Phys. Rev. B* **42**, 6268 (1990).
- [62] V. A. Gavrichkov, S. G. Ovchinnikov, A. A. Borisov, and E. G. Goryachev, *JETP* **91**, 369 (2000).
- [63] A. Sherman and M. Schreiber, *Phys. Rev. B* **50**, 12887 (1994).
- [64] E. L. Nagaev, *Phys. Rev. B* **64**, 144011 (2001).
- [65] V. Hizhnyakov and E. Sigmund, *Physica C* **156**, 655 (1988).

- [66] N. Voropajeva and A. Sherman, *Mod. Phys. Lett. B* **24**, 2327 (2010).
- [67] R. Matzdorf, Z. Fang, Ismail, J. Zhang, T. Kimura, Y. Tokura, K. Terakura, and E. W. Plummer, *Science* **289**, 746 (2000).
- [68] K. Maiti, D. D. Sarma, M. J. Rozenberg, I. H. Inoue, H. Makino, O. Goto, M. Pedio, and R. Cimino, *Europhys. Lett.* **55**, 246 (2001).

PUBLICATIONS

Curriculum Vitae

Niina Voropajeva

Date and place of birth: August 11, 1983, Ivangorod, Russia
Citizenship: Estonian
Address: Institute of Physics, University of Tartu,
Riia str. 142, 51014 Tartu, Estonia
E-mail: niina.voropajeva@ut.ee

Education

1989-1998 Secondary School No 4 of Narva
1998-2001 Narva Humanitarian Gymnasium
2001-2005 B.Sc. in physics, Faculty of Physics and Chemistry,
University of Tartu
2005-2007 M.Sc. in physics (theoretical physics), Faculty of Physics
and Chemistry, University of Tartu
2007-2011 PhD student, University of Tartu

Employment

02.2008-03.2009 Laboratory of Field Theory, Institute of Physics,
University of Tartu, engineer
04.2009-01.2010 Laboratory of Solid State Theory, Institute of
Physics, University of Tartu, engineer
02.2011- Laboratory of Solid State Theory, Institute of
Physics, University of Tartu, engineer

Scientific work

Main field of research: strongly correlated electron systems
Publications: 6 scientific articles

Teaching experience

- LOFY.04.037 Chaos and self-organization (lectures) (6 EAP),
2010/2011 fall
- LOFY.01.013 Practical Course in Physics III - Optics (4 EAP),
2010/2011 spring

Awards

2005 Estonian Academy of Sciences, II award from student research
contest (for bachelor thesis)
2010 Kaleva Travel scholarship

Curriculum Vitae in Estonian

Niina Voropajeva

Sünniaeg ja koht: 11. August, 1983, Ivangorod, Venemaa
Kodakondsus: Eesti
Aadress: Füüsika Insituut, Tartu Ülikool, Riia mnt. 142,
51014 Tartu, Eesti
E-mail: niina.voropajeva@ut.ee

Haridustee

1989-1998 Narva 4. Keskkool
1998-2001 Narva Humanitaargümnaasium
2001-2005 B.Sc. füüsikas, Tartu Ülikooli füüsika-keemia teaduskond
2005-2007 M.Sc. füüsikas (teoreetiline füüsika), Tartu Ülikooli
füüsika-keemia teaduskond
2007-2011 doktorant, Tartu Ülikool

Erialane teenistuskäik

02.2008-03.2009 Väljateooria labor, Füüsika Instituut,
Tartu Ülikool, insener
04.2009-01.2010 Tahkiseteooria labor, Füüsika Instituut,
Tartu Ülikool, insener
02.2011- Tahkiseteooria labor, Füüsika Instituut,
Tartu Ülikool, insener

Teadustegevus

Peamine töösund: tugevalt korreleeritud elektronsüsteemid
Publikatsioonid: 6 teaduslikki publikatsiooni

Õppetöö kogemus

- LOFY.04.037 Kaos ja iseorganiseerumine (loengud) (6 EAP),
2010/2011 sügissemester
- LOFY.01.013 Füüsika praktikum III - optika (4 EAP),
2010/2011 kevadsemester

Erialane tunnustus

2005 Eesti Teaduste Akadeemia üliõpilaste teadustööde konkursi
II preemia (bakalaureusetöö eest)
2010 Kaleva Traveli reisistipendium

DISSERTATIONES PHYSICAE UNIVERSITATIS TARTUENSIS

1. **Andrus Ausmees.** XUV-induced electron emission and electron-phonon interaction in alkali halides. Tartu, 1991.
2. **Heiki Sõnajalg.** Shaping and recalling of light pulses by optical elements based on spectral hole burning. Tartu, 1991.
3. **Sergei Savihhin.** Ultrafast dynamics of F-centers and bound excitons from picosecond spectroscopy data. Tartu, 1991.
4. **Ergo Nõmiste.** Leelishalogeniidide röntgenelektronemissioon kiiritamisel footonitega energiaga 70–140 eV. Tartu, 1991.
5. **Margus Rätsep.** Spectral gratings and their relaxation in some low-temperature impurity-doped glasses and crystals. Tartu, 1991.
6. **Tõnu Pullerits.** Primary energy transfer in photosynthesis. Model calculations. Tartu, 1991.
7. **Olev Saks.** Attoampri diapsoonis voolude mõõtmise füüsikalised alused. Tartu, 1991.
8. **Andres Virro.** AlGaAsSb/GaSb heterostructure injection lasers. Tartu, 1991.
9. **Hans Korge.** Investigation of negative point discharge in pure nitrogen at atmospheric pressure. Tartu, 1992.
10. **Jüri Maksimov.** Nonlinear generation of laser VUV radiation for high-resolution spectroscopy. Tartu, 1992.
11. **Mark Aizengendler.** Photostimulated transformation of aggregate defects and spectral hole burning in a neutron-irradiated sapphire. Tartu, 1992.
12. **Hele Siimon.** Atomic layer molecular beam epitaxy of A^2B^6 compounds described on the basis of kinetic equations model. Tartu, 1992.
13. **Tõnu Reinot.** The kinetics of polariton luminescence, energy transfer and relaxation in anthracene. Tartu, 1992.
14. **Toomas Rõõm.** Paramagnetic H^{2-} and F^+ centers in CaO crystals: spectra, relaxation and recombination luminescence. Tallinn, 1993.
15. **Erko Jalviste.** Laser spectroscopy of some jet-cooled organic molecules. Tartu, 1993.
16. **Alvo Aabloo.** Studies of crystalline celluloses using potential energy calculations. Tartu, 1994.
17. **Peeter Paris.** Initiation of corona pulses. Tartu, 1994.
18. **Павел Рубин.** Локальные дефектные состояния в CuO_2 плоскостях высокотемпературных сверхпроводников. Тарту, 1994.
19. **Olavi Ollikainen.** Applications of persistent spectral hole burning in ultrafast optical neural networks, time-resolved spectroscopy and holographic interferometry. Tartu, 1996.
20. **Ülo Mets.** Methodological aspects of fluorescence correlation spectroscopy. Tartu, 1996.
21. **Mikhail Danilkin.** Interaction of intrinsic and impurity defects in CaS:Eu luminophors. Tartu, 1997.

22. **Ирина Кудрявцева.** Создание и стабилизация дефектов в кристаллах KBr, KCl, RbCl при облучении ВУФ-радиацией. Tartu, 1997.
23. **Andres Osvet.** Photochromic properties of radiation-induced defects in diamond. Tartu, 1998.
24. **Jüri Örd.** Classical and quantum aspects of geodesic multiplication. Tartu, 1998.
25. **Priit Sarv.** High resolution solid-state NMR studies of zeolites. Tartu, 1998.
26. **Сергей Долгов.** Электронные возбуждения и дефектообразование в некоторых оксидах металлов. Tartu, 1998.
27. **Кауро Кукли.** Atomic layer deposition of artificially structured dielectric materials. Tartu, 1999.
28. **Ivo Heinmaa.** Nuclear resonance studies of local structure in $\text{RBa}_2\text{Cu}_3\text{O}_{6+x}$ compounds. Tartu, 1999.
29. **Aleksander Shelkan.** Hole states in CuO_2 planes of high temperature superconducting materials. Tartu, 1999.
30. **Dmitri Nevedrov.** Nonlinear effects in quantum lattices. Tartu, 1999.
31. **Rein Ruus.** Collapse of 3d (4f) orbitals in 2p (3d) excited configurations and its effect on the x-ray and electron spectra. Tartu, 1999.
32. **Valter Zazubovich.** Local relaxation in incommensurate and glassy solids studied by Spectral Hole Burning. Tartu, 1999.
33. **Indrek Reimand.** Picosecond dynamics of optical excitations in GaAs and other excitonic systems. Tartu, 2000.
34. **Vladimir Babin.** Spectroscopy of exciton states in some halide macro- and nanocrystals. Tartu, 2001.
35. **Toomas Plank.** Positive corona at combined DC and AC voltage. Tartu, 2001.
36. **Kristjan Leiger.** Pressure-induced effects in inhomogeneous spectra of doped solids. Tartu, 2002.
37. **Helle Kaasik.** Nonperturbative theory of multiphonon vibrational relaxation and nonradiative transitions. Tartu, 2002.
38. **Tõnu Laas.** Propagation of waves in curved spacetimes. Tartu, 2002.
39. **Rünno Lõhmus.** Application of novel hybrid methods in SPM studies of nanostructural materials. Tartu, 2002.
40. **Kaido Reivelt.** Optical implementation of propagation-invariant pulsed free-space wave fields. Tartu, 2003.
41. **Heiki Kasemägi.** The effect of nanoparticle additives on lithium-ion mobility in a polymer electrolyte. Tartu, 2003.
42. **Villu Repän.** Low current mode of negative corona. Tartu, 2004.
43. **Алексей Котлов.** Оксианионные диэлектрические кристаллы: зонная структура и электронные возбуждения. Tartu, 2004.
44. **Jaak Talts.** Continuous non-invasive blood pressure measurement: comparative and methodological studies of the differential servo-oscillometric method. Tartu, 2004.
45. **Margus Saal.** Studies of pre-big bang and braneworld cosmology. Tartu, 2004.

46. **Eduard Gerškevičš.** Dose to bone marrow and leukaemia risk in external beam radiotherapy of prostate cancer. Tartu, 2005.
47. **Sergey Shchemelyov.** Sum-frequency generation and multiphoton ionization in xenon under excitation by conical laser beams. Tartu, 2006.
48. **Valter Kiisk.** Optical investigation of metal-oxide thin films. Tartu, 2006.
49. **Jaan Aarik.** Atomic layer deposition of titanium, zirconium and hafnium dioxides: growth mechanisms and properties of thin films. Tartu, 2007.
50. **Astrid Rekker.** Colored-noise-controlled anomalous transport and phase transitions in complex systems. Tartu, 2007.
51. **Andres Punning.** Electromechanical characterization of ionic polymer-metal composite sensing actuators. Tartu, 2007.
52. **Indrek Jõgi.** Conduction mechanisms in thin atomic layer deposited films containing TiO₂. Tartu, 2007.
53. **Aleksei Krasnikov.** Luminescence and defects creation processes in lead tungstate crystals. Tartu, 2007.
54. **Küllike Rägo.** Superconducting properties of MgB₂ in a scenario with intra- and interband pairing channels. Tartu, 2008.
55. **Els Heinsalu.** Normal and anomalously slow diffusion under external fields. Tartu, 2008.
56. **Kuno Kooser.** Soft x-ray induced radiative and nonradiative core-hole decay processes in thin films and solids. Tartu, 2008.
57. **Vadim Boltrushko.** Theory of vibronic transitions with strong nonlinear vibronic interaction in solids. Tartu, 2008.
58. **Andi Hektor.** Neutrino Physics beyond the Standard Model. Tartu, 2008.
59. **Raavo Josepson.** Photoinduced field-assisted electron emission into gases. Tartu, 2008.
60. **Martti Pärs.** Study of spontaneous and photoinduced processes in molecular solids using high-resolution optical spectroscopy. Tartu, 2008.
61. **Kristjan Kannike.** Implications of neutrino masses. Tartu, 2008.
62. **Vigen Issahhanjan.** Hole and interstitial centres in radiation-resistant MgO single crystals. Tartu, 2008.
63. **Veera Krasnenko.** Computational modeling of fluorescent proteins. Tartu, 2008.
64. **Mait Müntel.** Detection of doubly charged higgs boson in the CMS detector. Tartu, 2008.
65. **Kalle Kepler.** Optimisation of patient doses and image quality in diagnostic radiology. Tartu, 2009.
66. **Jüri Raud.** Study of negative glow and positive column regions of capillary HF discharge. Tartu, 2009.
67. **Sven Lange.** Spectroscopic and phase-stabilisation properties of pure and rare-earth ions activated ZrO₂ and HfO₂. Tartu, 2010.
68. **Aarne Kasikov.** Optical characterization of inhomogeneous thin films. Tartu, 2010.

69. **Heli Valtna-Lukner.** Superluminally propagating localized optical pulses. Tartu, 2010.
70. **Artjom Vargunin.** Stochastic and deterministic features of ordering in the systems with a phase transition. Tartu, 2010.
71. **Hannes Liivat.** Probing new physics in e^+e^- annihilations into heavy particles via spin orientation effects. Tartu, 2010.
72. **Tanel Mullari.** On the second order relativistic deviation equation and its applications. Tartu, 2010.
73. **Aleksandr Lisovski.** Pulsed high-pressure discharge in argon: spectroscopic diagnostics, modeling and development. Tartu, 2010.
74. **Aile Tamm.** Atomic layer deposition of high-permittivity insulators from cyclopentadienyl-based precursors. Tartu, 2010.
75. **Janek Uin.** Electrical separation for generating standard aerosols in a wide particle size range. Tartu, 2011.
76. **Svetlana Ganina.** Hajusandmetega ülesanded kui üks võimalus füüsikaõppe efektiivsuse tõstmiseks. Tartu, 2011
77. **Joel Kuusk.** Measurement of top-of-canopy spectral reflectance of forests for developing vegetation radiative transfer models. Tartu, 2011.
78. **Raul Rammula.** Atomic layer deposition of HfO_2 – nucleation, growth and structure development of thin films. Tartu, 2011.
79. **Сергей Наконечный.** Исследование электронно-дырочных и интерстициал-вакансионных процессов в монокристаллах MgO и LiF методами термоактивационной спектроскопии. Тарту, 2011.